

# From Zero to Hero: How local curvature at artless initial conditions leads away from bad minima

Tony Bonnaire<sup>\*1</sup>, Giulio Biroli<sup>†1</sup>, and Chiara Cammarota<sup>‡2</sup>

<sup>1</sup>*Laboratoire de Physique de l'Ecole Normale Supérieure, ENS, Université PSL, CNRS, Sorbonne Université, Université Paris Cité, F-75005 Paris, France*

<sup>2</sup>*Dipartimento di Fisica, Sapienza Università di Roma and Istituto Nazionale di Fisica Nucleare, Sezione di Roma I, P. le A. Moro 5, 00185 Rome, Italy*

## Abstract

We provide an analytical study of the evolution of the Hessian during gradient descent dynamics, and relate a transition in its spectral properties to the ability of finding good minima. We focus on the phase retrieval problem as a case study for complex loss landscapes. We first characterize the high-dimensional limit where both the number  $M$  and the dimension  $N$  of the data are going to infinity at fixed signal-to-noise ratio  $\alpha = M/N$ . For small  $\alpha$ , the Hessian is uninformative with respect to the signal. For  $\alpha$  larger than a critical value, the Hessian displays at short-times a downward direction pointing towards good minima. While descending, a transition in the spectrum takes place: the direction is lost and the system gets trapped in bad minima. Hence, the local landscape is benign and informative at first, before gradient descent brings the system into an uninformative maze. Through both theoretical analysis and numerical experiments, we show that this dynamical transition plays a crucial role for finite (even very large)  $N$ : it allows the system to recover the signal well before the algorithmic threshold corresponding to the  $N \rightarrow \infty$  limit. Our analysis sheds light on this new mechanism that facilitates gradient descent dynamics in finite dimensions, and highlights the importance of a good initialization based on spectral properties for optimization in complex high-dimensional landscapes.

**Keywords:** Machine Learning | Phase Retrieval | Statistical Physics | Non-convex Optimization

## 1 Introduction

Minimization in non-convex and high-dimensional landscapes with possibly many minima is routinely performed in machine learning and optimization with great success by means of basic local iterative procedures like gradient descent or its stochastic variants. Understanding why, and to what extent, these procedures work is an open challenge to which a lot of studies were devoted recently. Without the aim of being exhaustive these include [45, 7, 30, 54, 38, 39, 1]. Several works have shown that actually spurious local minima are not present in certain regimes of parameters, in particular when the signal-to-noise ratio is large enough [51, 13]. So, despite their non-convexity, landscapes can become easy to descend. This would suggest an explanation of the success of gradient descent optimization based on the “trivialization” of the loss landscape [22], and the absence of bad minima. However, this cannot be the whole story, as it is known that bad minima are present in the regime of parameters where optimization succeeds [5, 26]. Theoretically, the study of gradient descent for matrix-tensor PCA [34], and later phase retrieval [36], offered a possible explanation. It showed that despite the presence of an exponential number (in the dimension  $N$ ) of bad minima, the dynamics can avoid them with probability one. The mechanism is related to the complexity of the loss landscape: what matters is when the bad minima with the largest basins of attraction become unstable towards the good ones, not when all the bad ones disappear. This “blessing” of dimension is due to the fact that the largest basins of attraction contain the initial conditions with probability one (up to corrections which are exponentially small in the dimension).

The present work focus on how the local curvature evolves during the descent, and how this affects optimization. Following [36], we focus on phase retrieval as a model for high-dimensional landscape, and on gradient flow as optimization dynamics. We characterize the evolution of the spectral properties of the Hessian during the dynamics, and show the emergence of a new phenomenon – a dynamical transition in the spectrum of the Hessian – which is crucial to characterize gradient descent dynamics.

---

<sup>\*</sup>tony.bonnaire@ens.fr

<sup>†</sup>giulio.biroli@ens.fr

<sup>‡</sup>chiara.cammarota@uniroma1.it

**Phase retrieval** The phase retrieval problem aims to recover a *signal*,  $\mathbf{w}^* \in \mathbb{R}^N$ , from the observation of  $M$  absolute projections of sensing vectors  $\mathbf{x}_i \in \mathbb{R}^N$  over it,  $\{|y_i|\}_{i=1}^M$ , with  $y_i = \mathbf{x}_i^\top \mathbf{w}^*$ . In our setting, the sensing vectors  $\{\mathbf{x}_i\}_{i=1}^M$  are considered i.i.d. Gaussian with zero mean and unit norm, and the signal is considered to be drawn on the  $N$ -sphere with  $\|\mathbf{w}^*\|_2 = \sqrt{N}$ . Despite its simplistic formulation, this problem appears in various scientific fields ranging from quantum chromodynamics to astrophysics [42, 24, 40, 50, 19, 58] and is known to be NP-hard in general [46]. This complexity led researchers to develop numerous algorithms relying on diverse approaches over the previous decade [16, 44, 55, 18, 62, 56, 57, 61]. A natural way of estimating a candidate vector  $\hat{\mathbf{w}}$  in the absence of any prior information is to specify a loss function  $\ell(y_i, \hat{y}_i)$  and optimize it iteratively through a gradient descent procedure starting from a random location in the parameter space, namely

$$\hat{\mathbf{w}}^{(t+1)} = \hat{\mathbf{w}}^{(t)} - \eta \nabla_{\hat{\mathbf{w}}^{(t)}} \mathcal{L}(\hat{\mathbf{w}}^{(t)}) + \eta \mu^{(t)} \hat{\mathbf{w}}^{(t)}, \quad (1)$$

where  $\mathcal{L}(\hat{\mathbf{w}}^{(t)}) = \frac{1}{2} \sum_{i=1}^M \ell(y_i, \hat{y}_i)$ ,  $\eta$  is a fixed learning rate,  $\hat{y}_i = \mathbf{x}_i^\top \hat{\mathbf{w}}^{(t)}$  is the  $i^{\text{th}}$  estimated label and  $\mu^{(t)} = \hat{\mathbf{w}}^{(t)} \cdot \nabla \mathcal{L}(\hat{\mathbf{w}}^{(t)})/N$  encodes the spherical constraint at each time step. Unless otherwise specified, the initial state is a random Gaussian vector,  $\hat{\mathbf{w}}^{(0)} \sim \mathcal{N}(\mathbf{0}_N, \mathbf{I}_N)$ .

**Teacher-student** Our analysis is performed in the teacher-student setup. One network, the *teacher*, generates a set of  $M$  measurements  $\{y_i\}_{i=1}^M$  using a signal  $\mathbf{w}^* \sim \mathcal{N}(\mathbf{0}_N, \mathbf{I}_N)$ . A second network with the same architecture, the *student*, exploits these measurements to estimate  $\mathbf{w}^*$  based on the procedure described by Eq. (1). We are interested in the generalization ability of the student as measured by the *magnetization*

$$m(t) = \frac{\hat{\mathbf{w}}^{(t)} \cdot \mathbf{w}^*}{N}, \quad (2)$$

taking value  $\pm 1$  when it produces an estimate  $\hat{\mathbf{w}}^{(t)}$  generalizing perfectly to new samples. In this paper, we call *equator* the set of states  $\hat{\mathbf{w}}^{(t)}$  having a magnetization of zero, containing for instance the initial random states when  $N \rightarrow \infty$ . There are various forms of loss functions studied in the literature. In order to avoid pathologies due to rare very large values of  $y_i$ , we focus on a normalized version of the intensity loss function defined as

$$\ell_a(y_i, \hat{y}_i) = \frac{(y_i^2 - \hat{y}_i^2)^2}{(a + y_i^2)}. \quad (3)$$

The role played by the normalization is important for the conditioning of Hessian eigenspectrum, in particular ensuring the existence of a hard left edge, a crucial element of our theoretical analysis. Although the precise values at which the transitions occur may vary with the choice of the loss function, we expect the physical mechanisms at hand and the interpretation we propose in this paper to generalize well to other loss functions. We provide evidences in Appendix D by varying  $a$ .

**Further prior works** It has been shown that for  $\alpha = M/N < \alpha_{\text{WR}} = 0.5$ , no estimator is able to obtain a generalization error better than a random guess while perfect recovery is achievable with the approximate message passing algorithm for  $\alpha > 1.13$  [6]. Many of the popular optimization methods developed over the past years rely on a careful initialization followed by an iterative algorithm in a form similar to Eq. (1). Such an initial guess is often provided by the leading eigenvector of a matrix function of the input data. This setup, and the transition associated to the spectral initialization in the high-dimensional limit  $M, N \rightarrow \infty$  with  $\alpha = M/N$  of order one, was studied in detail by several seminal previous works [6, 43, 29]. In particular, [43, 29] identify the optimal pre-processing matrix producing a non-zero overlap between its leading eigenvector and the signal when the sensing vectors are Gaussian. These results were later extended to the more generic unitary and orthogonal case in [32, 33], in which the optimal pre-processing is linked to a transition in the Hessian spectrum of the free energy landscape.

In parallel, several works have thoroughly investigated whether it is possible to retrieve the signal efficiently based on a random initialization. Sun et al. [52] show that when the entries are i.i.d. Gaussian, a number of  $O(N \log^3 N)$  samples trivializes the landscape making all minima become global, hence enabling traditional iterative methods to find a solution independently of the initialization. This threshold was later reduced to  $O(N)$  in [25, 14, 13] by adapting the form of the loss function, reducing the gap with the information-theoretic threshold of  $M = N$ .

Resorting to analogies with glassy dynamics of disordered systems, Mannelli et al. [36] argue that the convergence of a gradient descent algorithm is related to the trivialization of only a subset of bad minima. The dynamics is first trapped into peculiar high-energy bad minima, commonly called *threshold states* in the physics literature. When  $\alpha$  is large enough, these states develop a negative direction and a second descent

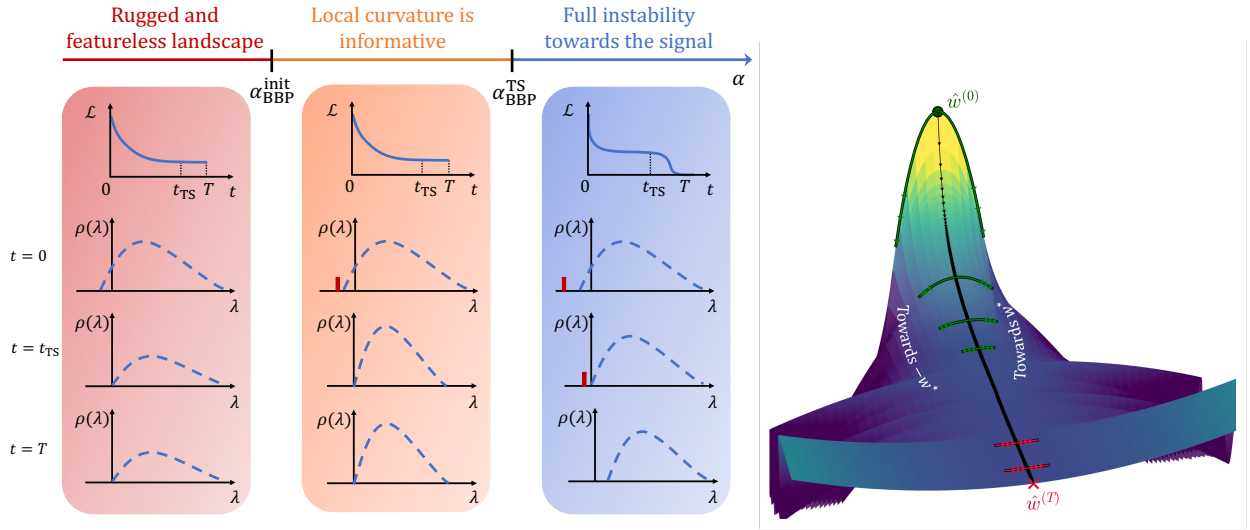


**Figure 1:** (Left) Phases of the gradient flow dynamics in the phase retrieval loss landscape for  $N \rightarrow \infty$ .  $\rho(\lambda)$  refers to the Hessian eigenvalue distribution, and the red bar shows when an outlier  $\lambda_*$  – and hence a descent direction towards  $\pm \mathbf{w}^*$  – exists. (Right) Evolution of the local curvature: dynamics projected in the direction of least stability  $\mathbf{v}_1^{(t)}$  of the Hessian matrix (black arrows) for  $\alpha = 2 \in [\alpha_{\text{BBP}}^{\text{init}}; \alpha_{\text{BBP}}^{\text{TS}}]$  and  $N = 256$ . Starting from an artless initial condition  $\hat{\mathbf{w}}^{(0)} \sim \mathcal{N}(\mathbf{0}_N, \mathbf{I}_N)$ , gradient descent reaches a bad minimum. The green arrows indicate downward directions towards  $\pm \mathbf{w}^*$  during the dynamics. At the end, the local curvature has become positive (red arrows).

phase occurs throughout a locally convex basin until a global minimum is reached, hence converging to  $\pm \mathbf{w}^*$ . The transition between the two phases is governed by an eigenvalue popping out of the continuous bulk of the otherwise-marginal Hessian spectrum, a phenomenon dubbed *Baik-Ben Arous-Pêché* (BBP) transition. A similar phenomenon arises in several random matrix problems ranging from physics and ecology to finance and computer science [49, 12, 34, 37, 20].

The teacher-student setting that we study is a particular case of learning a single-index model in which we assume the activation function of the teacher to be known to the student. These models received much attention these past years [3, 8, 9, 2, 11], essentially to understand the dynamics of (online) stochastic gradient descent in the loss landscape.

**Contributions** Although the spectral properties of the loss Hessian are conjectured to play a role during the gradient descent dynamics, there are no analytical results characterizing the dynamical evolution of the Hessian and connecting it to the dynamics. Here, we fill this gap focusing on phase retrieval as a model for non-convex high-dimensional training dynamics with  $N, M \rightarrow \infty$ , and at fixed signal-to-noise ratio  $\alpha = M/N \sim O(1)$ . We show the existence of different regimes depending on  $\alpha$  that are linked to the smallest eigenvalue  $\lambda_1$  of the Hessian (see the left panel of Fig. 1):

- I. *Rugged and featureless landscape:* When  $\alpha < \alpha_{\text{BBP}}^{\text{init}}$ , random initial conditions have no direction correlated with  $\pm \mathbf{w}^*$ . The dynamics is unable to find the signal back and gets stuck into high-loss minima that are marginally stables (i.e., with a vanishing smallest eigenvalue  $\lambda_1$ ), called threshold states;
- II. *Local curvature is informative & dynamical transition in the Hessian:* When  $\alpha \in [\alpha_{\text{BBP}}^{\text{init}}; \alpha_{\text{BBP}}^{\text{TS}}]$ , any initial condition  $\hat{\mathbf{w}}^{(0)}$  sits in a region of the landscape with a downward direction pointing towards the signal. More formally, the eigenvector  $\mathbf{v}_1$  of the initial Hessian associated to  $\lambda_1$  has a finite overlap with  $\mathbf{w}^*$ . However, during the gradient descent, the direction  $\mathbf{v}_1^{(t)}$  rotates away from the signal and, at a finite time, the correlation is lost. Hence, the system does not have enough time to head towards the signal, and the dynamics gets once again trapped into bad minima (threshold states), as illustrated in the right panel of Fig. 1;
- III. *Full instability towards the signal:* When  $\alpha > \alpha_{\text{BBP}}^{\text{TS}}$ , the threshold states turn from local minima to saddle-points that have exactly one negative direction pointing towards the signal, making gradient descent converge to a well-generalizing (global) minimum in the second phase of the dynamics, when  $t \geq t_{\text{TS}}$ , defined as the time required to reach a threshold state.

These findings, that we obtain in the high-dimensional  $N \rightarrow \infty$  limit, have crucial consequences for finite but large dimensions. In regime II, the local curvature towards the good minima is negative at the beginning of the dynamics and positive at the very end, as shown in the right panel of Fig. 1. For  $N \rightarrow \infty$ , the system

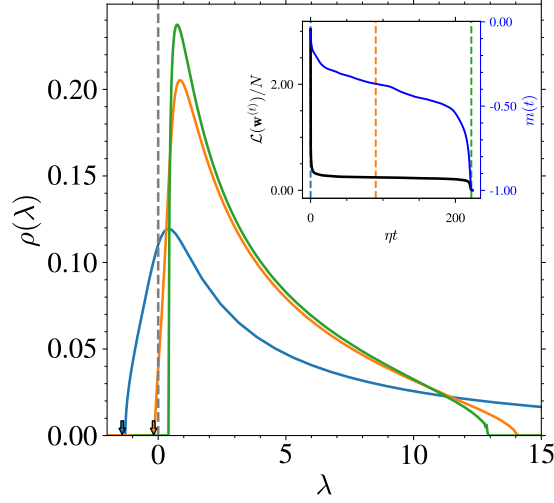


**Figure 2:** Hessian eigenvalue distribution  $\rho(\lambda)$  of a successful simulation with  $N = 2048$  and  $\alpha = 3.1$ . The inset shows the evolution of the rescaled loss function  $\mathcal{L}(\hat{\mathbf{w}}^{(t)})/N$  (black curve) and the magnetization  $m(t)$  (blue curve). Colored lines for eigenvalue distributions refer to different times shown in the inset. Arrows indicate the minimum eigenvalue when it is isolated from the bulk.

takes a time of order  $\log N$  to escape the equator in presence of an unstable direction<sup>1</sup>. Hence, before being able to escape the equator, the dynamics gets trapped in the threshold states, and cannot recover the signal until  $\alpha$  becomes larger than  $\alpha_{\text{BBP}}^{\text{TS}}$ . Nevertheless, for finite – even very large –  $N$ , the initial descent direction can be exploited to acquire, in the relatively short timescale  $\log N$ , a finite correlation with the signal before getting trapped in the threshold states. This finite-dimensional effect disappears only logarithmically with  $N$  meaning it should lead to an effective transition growing with  $\log N$ . This phenomenon is therefore very relevant for practical applications, and explains the large *negative* gap reported in [36] between the value of  $\alpha$  computed for  $N \rightarrow \infty$  and the empirical success rates obtained from numerical simulations with finite  $N$ .

This picture we draw of the phase retrieval landscape at the equator completes the seminal one presented in Mannelli et al. [36] in which only regimes I and III are identified. It also highlights the importance of a good initialization for optimization in high-dimensional non-convex landscapes, in particular by spectral methods (the Hessian initialization being a particular case). In order to showcase this effect, it was crucial to study a model with a complex landscape such as phase retrieval since it is not present in simpler problems like the matrix-tensor PCA [35]. Our results are established by a detailed analytical study of the spectral properties of the Hessian, in particular the associated BBP transition (Sect. 3) and confirmed by suitably designed numerical experiments in Sect. 4.

## 2 A motivating example

To illustrate the phenomenon we will analyze later, let us focus on a numerical example of a trajectory in the intermediate regime II where  $\alpha \in [\alpha_{\text{BBP}}^{\text{init}}, \alpha_{\text{BBP}}^{\text{TS}}]$ . It is displayed in Figure 2 with the evolution of the eigenspectrum at several timesteps during a successful realization of gradient descent initialized randomly for  $\alpha = 3.1$  and  $N = 2048$ . The inset highlights two dynamical regimes. First, the loss function quickly decreases to reach a plateau in which the system gets stuck for most of the simulation time. Second, a descent phase where it finally escapes the saddle-point and the loss reaches zero. While the system iteratively moves towards a low loss value, the Hessian displays a single negative eigenvalue in the direction of the signal (blue and orange arrows). As we will see analytically in Sect. 3, the local curvature towards the signal is negative from the very beginning of the dynamics (blue arrow). The system therefore exploits this direction and eventually reaches a global minimum with all positive eigenvalues (green curve), and a magnetization  $m(T) = -1$ , before getting trapped in the threshold states that would be stable at this value of  $\alpha$ . The evolution of  $m(t)$  in the inset – growing while the loss is decreasing – is in fact due to this phenomenon of initial negative local curvature that is exploited when  $N$  is finite, allowing the magnetization to grow from its initial value on timescales of order  $\log N$ . This mechanism moves the system away from the equator where the landscape is easier to descend [48], in turn enabling gradient descent to succeed and find back the signal  $-\mathbf{w}^*$  in a regime of  $\alpha$  where bad minima are still present at the equator.

<sup>1</sup>The magnetization grows exponentially but is of order  $1/\sqrt{N}$  at the beginning, see [3, 10, 2].

### 3 Theory of the BBP transitions in the phase retrieval loss landscape

#### 3.1 Method: Hessian eigenspectrum and BBP condition

Here we present the theoretical analysis which enables us to obtain the spectral properties of the Hessian during the gradient descent dynamics. The Hessian matrix associated to the phase retrieval optimization is of the form

$$\mathcal{H}(\hat{\mathbf{w}}^{(t)}) = \sum_{i=1}^M f(y_i, \hat{y}_i) \mathbf{x}_i \mathbf{x}_i^\top - \mu^{(t)} \mathbf{I}_N, \quad (4)$$

with  $f(y_i, \hat{y}_i) = \partial_{\hat{y}_i}^2 \ell_a(y_i, \hat{y}_i)$ , and  $\mathbf{I}_N$  the identity matrix of size  $N \times N$ . In what follows, we omit the spherical constraint without any loss of generality since it simply induces a shift of the eigenvalues by  $\mu^{(t)}$ . When considering the data vectors  $\mathbf{x}_i$  as i.i.d. Gaussian,  $\mathcal{H}(\hat{\mathbf{w}}^{(t)})$  is actually a random matrix drawn from what is called the *non-white Wishart ensemble* [47]. We are interested in characterizing the value of  $\alpha$  at which the smallest eigenvalue of the Hessian, that we denote  $\lambda_*$ , detaches from the bulk and its associated eigenvector has a finite scalar product with the signal. In this case,  $\lambda_*$  creates an outlier as seen in of the left panel of Fig. 1 (red bars). This transition of the smallest eigenvalue is called BBP transition [4] and can be characterized analytically. Resorting to the tools from random matrix theory, we derive equations for the behavior of the border of the bulk and the outlier eigenvalue  $\lambda_*$ . Following Appendix A.1 and results in [27], it yields that the transition value of  $\alpha$ , referred to as  $\alpha_{\text{BBP}}$ , satisfies

$$\lambda_* = \alpha_{\text{BBP}} \mathbb{E}_{y, \hat{y}} \left[ \frac{f(y, \hat{y}) y^2}{1 - f(y, \hat{y}) \mathcal{S}_-} \right], \quad (5)$$

$$\mathcal{S}_- = \alpha_{\text{BBP}} \mathbb{E}_{y, \hat{y}} \left[ \frac{f(y, \hat{y})^2}{(1 - f(y, \hat{y}) \mathcal{S}_-)^2} \right]. \quad (6)$$

We provide in Appendix A.2 numerical evidences that these equations give accurate predictions of the spectrum of matrices in the form of Eq. (4), even at finite  $N$ . When  $\alpha > \alpha_{\text{BBP}}$ , the eigenvector  $\mathbf{v}_1$  associated to the smallest eigenvalue  $\lambda_1 = \lambda_*$  of the Hessian matrix  $\mathcal{H}(\hat{\mathbf{w}}^{(t)})$  displays a non-zero overlap with the signal  $\pm \mathbf{w}^*$  that can also be obtained (see Appendix A.3) as

$$(\mathbf{v}_1 \cdot \mathbf{w}^*)^2 = \frac{1}{1 - \partial_z \Sigma(z)|_{z=\lambda_*}}, \quad (7)$$

where

$$\Sigma(z) = \alpha \mathbb{E}_{y, \hat{y}} \left[ \frac{f(y, \hat{y}) y^2}{1 - f(y, \hat{y}) \mathcal{S}_\mathcal{H}(z)} \right]. \quad (8)$$

The BBP condition, as well as the squared overlap  $(\mathbf{v}_1 \cdot \mathbf{w}^*)^2$ , are consequently expressed in terms of expectations computed over the joint probability distribution of the true and estimated labels at time  $t$ ,  $p(y, \hat{y}, t)$ . Once the latter is known, one can solve the self-consistent Eqs. (5) and (6) to obtain the value of  $\alpha_{\text{BBP}}$ , where  $\mathbf{v}_1$  develops a non-zero correlation with signal characterized by Eq. (7). The rest of this section is devoted to analyze for which values of  $\alpha$  and  $t$  the BBP transition takes place.

#### 3.2 BBP transition at initialization

In the case of i.i.d. Gaussian measurements  $y_i$ , and before operating the gradient descent,  $p(y, \hat{y}, 0)$  is the product of two Gaussian distributions. The aforementioned equations characterizing the BBP transition can therefore be solved to obtain the value  $\alpha_{\text{BBP}}^{\text{init}} = 1.13$  for the considered loss function  $\ell_{a=1}$ . As a consequence, whenever  $\alpha > \alpha_{\text{BBP}}^{\text{init}}$ , any initial condition  $\hat{\mathbf{w}}^{(0)}$  is characterized by a Hessian spectrum with an isolated left-most eigenvalue and an eigenvector  $\mathbf{v}_1$  pointing towards the signal  $\pm \mathbf{w}^*$ . More precisely, it has a finite overlap with the signal that grows with the value of  $\alpha$ , which can be computed from Eq. (7), and displayed as the dashed line in the left panel of Fig. 3.

#### 3.3 BBP transition on threshold states

The characterization of  $p(y, \hat{y}, t_{\text{TS}})$  is more involved than at initialization (note that  $t_{\text{TS}} = \infty$  when  $N \rightarrow \infty$ ). Right after a single step of gradient descent,  $y$  and  $\hat{y}$  are correlated. To pursue our analysis, we employ two methods allowing to approximate this joint distribution: (i) through adapted numerical simulations



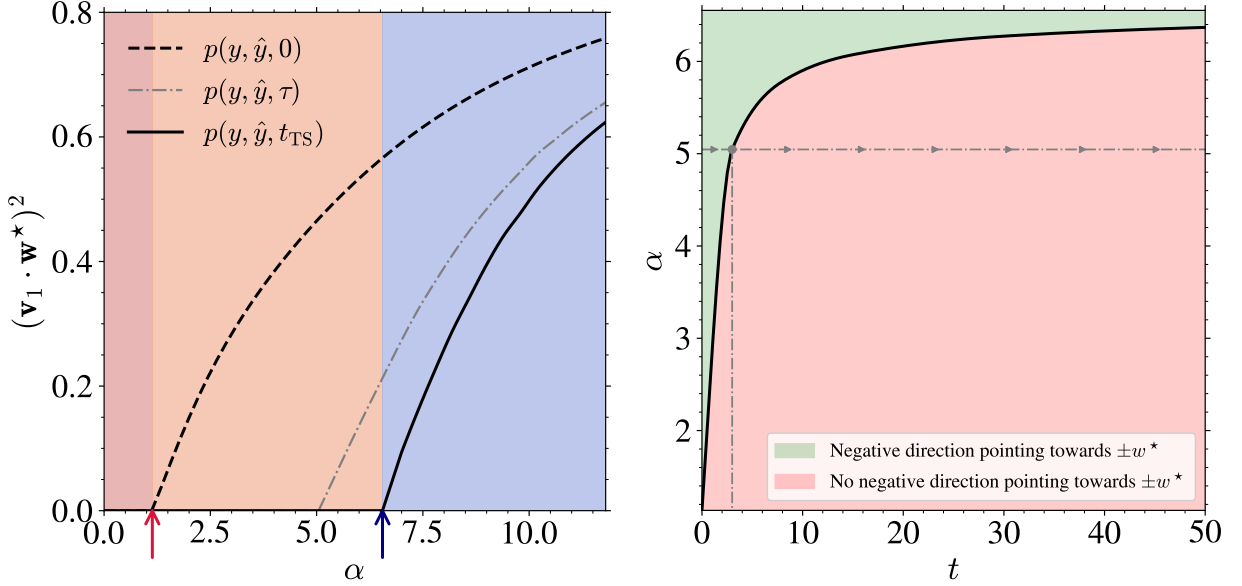


**Figure 3: Dynamical BBP theory at the equator of the phase retrieval loss landscape for  $N \rightarrow \infty$ .** (Left) Evolution of  $(v_1 \cdot w^*)^2$  from Eq. 7 at initialization (dashed line), on threshold states (solid line), and at an intermediary time  $\tau \in [0, t_{TS} = \infty]$  (grey dashed-dotted line). The red (resp. blue) arrow indicates  $\alpha_{BBP}^{init} = 1.13$  (resp.  $\alpha_{BBP}^{TS} = 6.55$ ). The background colors refer to the three different regimes introduced in Fig. 1. (Right) Dynamical phase diagram of the value of  $\alpha$  required for a BBP transition to take place with the descent time  $t$ . The grey dashed-dotted line refers to the intermediate time  $\tau$  of the left panel. In both plots, the loss function is the one of Eq. (3) with  $a = 1$ .

(described more precisely in Sect. 4) sampling the threshold states. One can then evaluate empirically the expectations of Eqs. (5) and (6); (ii) through the statistical physics of disordered systems and the replica method (see Appendix B), as performed in [21, 36]. Those two methods grant us two consistent but different values of the BBP transition on threshold states that are respectively  $\alpha_{BBP}^{TS} = 6.55$  and  $\alpha_{BBP}^{1RSB,TS} = 6.9$ . We expect the gap between these two values to vanish when moving to more accurate RSB schemes and we adopt  $\alpha_{BBP}^{TS}$  as the BBP threshold for the rest of the paper. For  $\alpha > \alpha_{BBP}^{TS}$ , also the threshold states turn from minima to saddles and develop a negative direction pointing towards  $\pm w^*$ : the overlap of the corresponding eigenvector with  $\pm w^*$  is shown as the solid line in the left panel of Fig. 3.

### 3.4 Dynamical BBP transitions

Comparing the evolution of the overlaps at  $t = 0$  and  $t = t_{TS}$  in the left panel of Fig. 3, we find that gradient descent transports the initial state towards a location that is in an even rougher part of the landscape, and that does *not* allow recovery in the entire intermediate region of  $\alpha$  (as also illustrated in the right panel of Fig. 1). For a given  $\alpha$  such that  $\alpha_{BBP}^{init} < \alpha < \alpha_{BBP}^{TS}$ , and at a finite time  $t_{BBP}(\alpha)$ , a BBP transition takes place during the descent as the informative isolated eigenvalue enters the bulk distribution, as illustrated by the dashed-dotted line and arrows from the right panel of Fig. 3. The two ideal limits discussed above corresponds to  $t_{BBP}(\alpha_{BBP}^{init}) = 0$  and  $t_{BBP}(\alpha_{BBP}^{TS}) = \infty$  but the same endeavor can be pursued for intermediate descent times. For instance, Fig. 3 reveals that for  $\alpha \approx 5.05$ , an initial negative local curvature pointing towards the signal exists until a finite descent time of  $t_{BBP}(\alpha) = 3$  when it disappears, thus preventing signal recovery.

### 3.5 Finite $N$ dynamics

So far, the results of this section are obtained in the  $N \rightarrow \infty$  limit. When  $N$  is finite but large, the initial magnetization  $m(t = 0)$  in the downward direction towards the signal is of order  $1/\sqrt{N}$ , as a consequence of the high-dimensional nature of our analysis and the central limit theorem. In the intermediate regime of  $\alpha$ , the component along this direction is therefore expected to grow exponentially (due to the negative curvature) but with a prefactor  $1/\sqrt{N}$ , i.e.  $m(t) \approx \exp(ct)/\sqrt{N}$  with  $c$  a constant associated to the local curvature at initialization. In consequence, a time of order  $\log N$  is needed to acquire a component of order one in the direction of the signal. For  $N \rightarrow \infty$ , and  $\alpha_{BBP}^{init} < \alpha < \alpha_{BBP}^{TS}$ , this time diverges and the system loses the negative local curvature before actually being able to use it, as shown in the right panel of Fig. 3 where the negative curvature towards  $\pm w^*$  is lost in finite times. However, this happens only in the strict

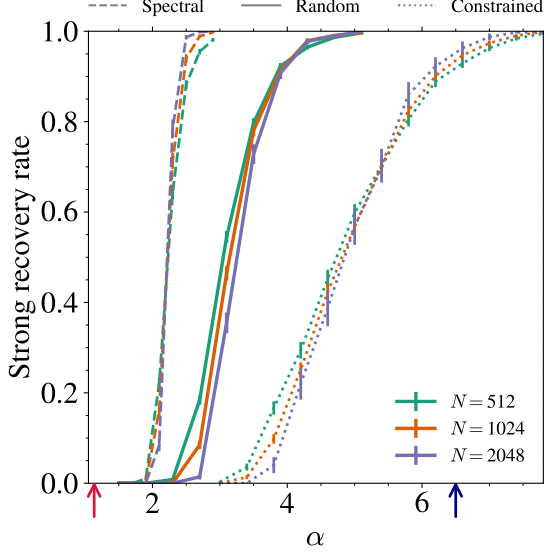


**Figure 4:** Strong recovery rates as a function of  $\alpha$  for several values of  $N$  and types of initializations: spectral, random, or constrained. The red (resp. blue) arrow indicates  $\alpha_{\text{BBP}}^{\text{init}}$  (resp.  $\alpha_{\text{BBP}}^{\text{TS}}$ ). The error bars represent 95% confidence intervals on the average.

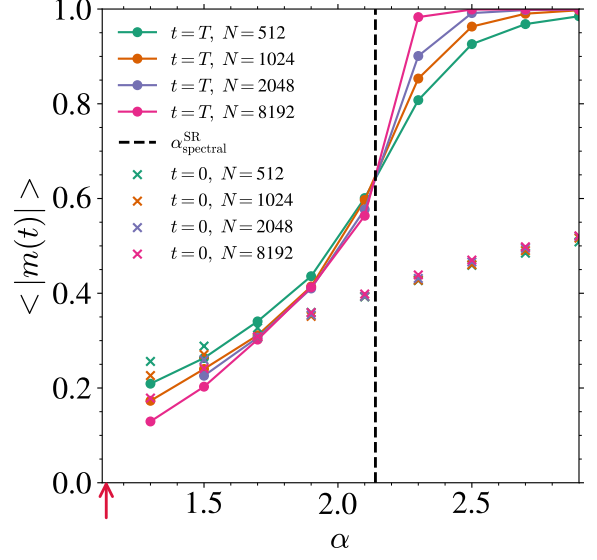


**Figure 5:** Evolution of the averaged absolute magnetization  $\langle |m(t)| \rangle$  with  $\alpha$  for several values of  $N$  at times 0 and  $T$  using spectral initialization along  $v_1$ . The red arrow denotes  $\alpha_{\text{BBP}}^{\text{init}}$  and the vertical dashed black line corresponds to the strong recovery threshold  $\alpha_{\text{spectral}}^{\text{SR}}$ .

large  $N$  limit. For finite, and even very large,  $N$  the situation changes substantially, as  $\log N$  is not such a large time-scale. In consequence, the system can acquire a magnetization  $m(t)$  of order one before hitting the dynamical BBP transition where the descent direction is lost, and hence avoid the bad minima. This should lead to a finite- $N$  algorithmic transition well below  $\alpha_{\text{BBP}}^{\text{TS}}$ , even for very large  $N$ .

This phenomenon therefore plays a crucial role in practice by moving the system away from the equator during the descent, where the loss landscape is expected to become more benign [48], therefore enabling early-on successes when  $N$  is finite. This was for instance hinted in Sect. 2 and Fig. 2, where the inset shows the growth of the magnetization  $m(t)$  from  $1/\sqrt{N}$  to values of order one while the loss decreases and plateaus. As  $|m(t)|$  increases,  $\hat{w}^{(t)}$  reaches a threshold state of large latitude ( $m(t_{\text{TS}}) \approx 0.4$ ) having a descending direction pointing to  $-w^*$  (orange arrow) that is enabling recovery, despite the bad minima at the equator that remain stables until  $\alpha_{\text{BBP}}^{\text{TS}}$ . In the following, we test these hypotheses for finite  $N$  through numerical experiments.

## 4 Numerical analysis of the gradient descent dynamics

We run multiple experiments to analyze the behavior of gradient descent initialized both randomly and spectrally at finite values of  $N$ . To do so, we solve Eq. (1) at fixed learning rate  $\eta = 6 \times 10^{-3}$  for  $T = 9000 \log_2(N)$  steps starting from different states depending on the initialization scheme. The effect of the learning rate on the numerical results is tested in Appendix C. We also consider a system to perform strong recovery (meaning that  $m(T) = \pm 1$ ) whenever  $|m(T)| \geq 0.99$ .

First, let us focus on randomly initialized weights  $\hat{w}^{(0)} \sim \mathcal{N}(\mathbf{0}_N, \mathbf{I}_N)$ , leading to the strong recovery rates shown as solid lines in Fig. 4 for  $N \in \{512, 1024, 2048\}$ . We observe, in agreement with the previous arguments, that the simulations achieve strong recovery well before  $\alpha_{\text{BBP}}^{\text{TS}}$ , without clearly intersecting each other. This gap between the simulations and the BBP prediction obtained from infinite-dimensional arguments was also observed in [36]. As discussed in the previous Sect. 3.4, it is due to the displacement of the effective transition logarithmically with  $N$  (see also Appendix C). In what follows, we devise more elaborated ways of exploring the landscape to bypass this effect.

### 4.1 A constrained optimization to probe threshold states

Efficiently sampling the threshold states numerically at finite  $N$  is a critical aspect of our numerical analysis to show that:

1. These states exist in the phase retrieval loss landscape,

2. Gradient descent initialized randomly is trapped into them,

3. They are responsible for the BBP transition at the end of the dynamics for  $N \rightarrow \infty$ .  
In order to sample the threshold states, we constrain the optimization to remain at the equator. In practice, we project the estimate at each time step  $t$  in the subspace orthogonal to  $w^*$  as

$$\hat{w}_{\perp}^{(t)} = \left( I_N - \frac{w^* w^{*\top}}{N} \right) \hat{w}^{(t)}, \quad (9)$$

where  $\hat{w}^{(t)}$  is defined in Eq. (1). While sticking to the equator, the loss is still gradually decreased until it reaches a plateau as in Fig. 2, but with an enforced magnetization of zero. In practice, we perform  $t_c = 60\,000$  gradient descent steps with the constraint and converge to a state  $\hat{w}^{(t_c)}$  that we use as initialization for the standard gradient descent in a procedure called *constrained initialization*. Note however that this numerical scheme is not properly sampling the threshold states since the gradient cannot be zero in the direction of the signal (its component is however  $\sqrt{N}$  smaller than the gradient norm). We have checked numerically that the states we visit have the expected properties (marginal Hessian, BBP transition at the right  $\alpha$ , and eigenvalues behave as expected from Sect. 3).

We show as the dotted lines in Fig. 4 the strong recovery rates obtained with constrained initialization. Contrary to what we observed in the case of random initialization, the successes for different values of  $N$  now seem to converge at around  $\alpha_{\text{cons.}}^{\text{SR}} \approx 5.5$ . While this value is still not matching perfectly the high-dimensional prediction  $\alpha_{\text{BBP}}^{\text{TS}} = 6.55$ , it shifts the success rates to larger  $\alpha$  with respect to the random initialization case. This means in particular that the threshold states exist at the equator and they indeed are found in a rougher part of the landscape, making it harder to converge to a well-generalizing minimum, as predicted from the theory of Sect. 3. We leave to future works to solve the numerical discrepancy found above between  $\alpha_{\text{cons.}}^{\text{SR}}$  and  $\alpha_{\text{BBP}}^{\text{TS}}$ , which could be due to additional strong finite size effects.

## 4.2 Spectral initialization, weak recovery and loss landscape away from the equator

As stated in Sect. 3, when  $\alpha > \alpha_{\text{BBP}}^{\text{init}}$ , the Hessian matrix of any random configuration  $\hat{w}^{(0)}$  has a direction of least stability  $v_1$  displaying a non-zero overlap with the signal. This idea is at the heart of what is called *spectral initialization* proposed and studied in many previous works [16, 57, 6, 43, 28, 32, 33]. By initializing the descent at  $\hat{w}^{(0)} = v_1$ , one expects the system to avoid the bad minima, or at least to reach threshold states of larger latitudes that may exhibit a BBP transition at a lower signal-to-noise ratio  $\alpha$ . From the perspective discussed in the previous sections, initializing along  $v_1$  is like taking fully advantage of the negative local curvature from the very beginning of the gradient descent. The dashed lines of Fig. 4 support numerically these intuitions with a strong recovery transition occurring around  $\alpha_{\text{spectral}}^{\text{SR}} \approx 2.14 < \alpha_{\text{random}}^{\text{SR}}$ . This is also emphasized by Fig. 5 in which we plot the evolution of the averaged magnetizations both at initialization along  $v_1$  (crosses) and after  $T$  steps of gradient descent (dots and solid lines).

There are several important findings associated to Fig. 5. First, there is a regime  $\alpha_{\text{BBP}}^{\text{init}} < \alpha < \alpha_{\text{spectral}}^{\text{SR}}$  in which Hessian initialization leads to weak recovery (meaning it reaches states that have a finite magnetization  $|m(T)| < 0.99$  in practice), and a regime  $\alpha > \alpha_{\text{spectral}}^{\text{SR}}$  in which it leads to strong recovery ( $|m(T)| \geq 0.99$ ). This hints at a complex characterization of the loss landscape away from the equator, with minima still trapping the dynamics at low  $\alpha$  but having a finite magnetization, see [41] for related results and [48] for a Kac-Rice perspective on simpler models. Second, Fig. 5 shows that indeed by using the initial local negative curvature the system can achieve strong recovery well below  $\alpha_{\text{BBP}}^{\text{TS}}$ . These results therefore highlight the importance of a good initialization for gradient descent dynamics, especially in regimes as the ones found here, in which the landscape is more benign at the beginning of the dynamics than later on.

## 5 Discussion and perspectives

In this paper, we provide a theoretical study of the behavior of gradient descent in a high-dimensional and non-convex landscape through the Gaussian noiseless phase retrieval problem in a teacher-student setup. Based on the analytical and dynamical description of the Hessian spectrum during the descent, we are able to understand the main conditions of success and failure of gradient descent in the high-dimensional limit  $N, M \rightarrow \infty$  with respect to  $\alpha = M/N \sim O(1)$ . From this analysis, we draw several conclusions and perspectives for phase retrieval at both finite and infinite  $N$ .



**The local landscape is more benign and informative at the beginning of the dynamics.** The value of  $\alpha$  required to induce a BBP transition of the Hessian matrix towards the signal is larger on threshold states than at random initialization. However, for  $N \rightarrow \infty$ , although there exists one descending direction going towards  $\pm \mathbf{w}^*$  at  $t = 0$ , gradient descent ignores it and ends up being trapped by the threshold states when  $\alpha \in [\alpha_{\text{BBP}}^{\text{init}}, \alpha_{\text{BBP}}^{\text{TS}}]$ . A much larger signal-to-noise ratio is required to render the latter unstable.

**Finite  $N$  random initializations benefit from this phenomenon.** Due to the initial local curvature towards  $\pm \mathbf{w}^*$  existing at  $\alpha > \alpha_{\text{BBP}}^{\text{init}} = 1.13$ , and to the finite value of  $N$  used in practice, the magnetization  $m(t)$  between the estimate and the signal is able to grow during the descent. This enables the system to escape the equator on a timescale of order  $\log N$  by leaving the rough part of the landscape and join benign regions. This is the mechanism that allows for successful optimization in practice, well before the algorithmic threshold corresponding to the high-dimensional limit  $N \rightarrow \infty$ .

**The importance of spectral initializations.** Given that the landscape is more benign at the beginning of the dynamics, spectral initializations can be very useful to escape more efficiently from the equator before reaching the bad region. This phenomenon provides a showcase for a strong advantage of spectral initializations and, more generally, of spectral properties to improve optimization in non-convex and high-dimensional landscape – a research direction that received a lot of attention recently in the context of deep learning [23, 53, 59]. Our theoretical analysis of the BBP transitions holds at the equator, where  $m = 0$ . To get a better understanding of spectral initializations, one must study the topological properties of the landscape as a function of both  $\alpha$  and  $m$ . This could be done using the Kac-Rice method for loss functions in the form of Eq. (3) as proposed in [31].

**Not all loss functions are equal.** The values of  $\alpha$  at which the dynamical BBP transitions occur depend strongly on the choice of the loss function. Thus, it would be interesting to find losses that enhance this phenomenon and lead to an earlier signal recovery, as done in [43] for spectral initializations and in [13, 15] for landscape trivialization. Finally, it would be worth characterizing this phenomenon for a broader class of loss functions. We show a first case study by varying  $a$  in Eq. (3) in Appendix D.

## Acknowledgments

The authors thank Stefano Sarao Mannelli for sharing his code used in [36]. T.B. further thanks Aurélien Decelle and Bruno Loureiro for useful discussions on the topic. G.B. acknowledges support from the French government under the management of the Agence Nationale de la Recherche as part of the “Investissements d’avenir” program, reference ANR-19-P3IA0001 (PRAIRIE 3IA Institute). C.C. acknowledges financial support from PNR MUR project PE0000013-FAIR and from MUR through PRIN2022 project 202234LKBW-Land(e)scapes.

## References

- [1] Annesi, B. L., Lauditi, C., Lucibello, C., Malatesta, E. M., Perugini, G., Pittorino, F., and Saglietti, L. Star-shaped space of solutions of the spherical negative perceptron. *Phys. Rev. Lett.*, 131:227301, Nov 2023. doi: 10.1103/PhysRevLett.131.227301. URL <https://link.aps.org/doi/10.1103/PhysRevLett.131.227301>.
- [2] Arnaboldi, L., Krzakala, F., Loureiro, B., and Stephan, L. Escaping mediocrity: how two-layer networks learn hard single-index models with sgd. *arXiv preprint arXiv:2305.18502*, 5 2023. URL <http://arxiv.org/abs/2305.18502>.
- [3] Arous, G. B., Gheissari, R., and Jagannath, A. Online stochastic gradient descent on non-convex losses from high-dimensional inference. *Journal of Machine Learning Research*, 22(106):1–51, 2021. URL <http://jmlr.org/papers/v22/20-1288.html>.
- [4] Baik, J., Arous, G. B., and Pécché, S. Phase transition of the largest eigenvalue for nonnull complex sample covariance matrices. *Annals of Probability*, 33:1643–1697, 2005. ISSN 00911798. doi: 10.1214/009117905000000233.

- [5] Baity-Jesi, M., Sagun, L., Geiger, M., Spigler, S., Arous, G. B., Cammarota, C., LeCun, Y., Wyart, M., and Biroli, G. Comparing dynamics: deep neural networks versus glassy systems. *Journal of Statistical Mechanics: Theory and Experiment*, 12:124013, 2019. ISSN 02017563. doi: 10.1088/1742-5468/ab3281. URL <https://ui.adsabs.harvard.edu/abs/2019JSMTE..12.4013B>.
- [6] Barbier, J., Krzakala, F., Macris, N., Miolane, L., and Zdeborová, L. Optimal errors and phase transitions in high-dimensional generalized linear models. *Proceedings of the National Academy of Sciences of the United States of America*, 116:5451–5460, 2019. ISSN 10916490. doi: 10.1073/pnas.1802705116.
- [7] Belkin, M., Ma, S., and Mandal, S. To understand deep learning we need to understand kernel learning. In Dy, J. and Krause, A. (eds.), *Proceedings of the 35th International Conference on Machine Learning*, volume 80 of *Proceedings of Machine Learning Research*, pp. 541–549. PMLR, 10–15 Jul 2018. URL <https://proceedings.mlr.press/v80/belkin18a.html>.
- [8] Ben Arous, G., Gheissari, R., and Jagannath, A. High-dimensional limit theorems for SGD: Effective dynamics and critical scaling. In Oh, A. H., Agarwal, A., Belgrave, D., and Cho, K. (eds.), *Advances in Neural Information Processing Systems*, 2022. URL <https://openreview.net/forum?id=Q38D6xxrKHe>.
- [9] Bietti, A., Bruna, J., Sanford, C., and Song, M. J. Learning single-index models with shallow neural networks. In Oh, A. H., Agarwal, A., Belgrave, D., and Cho, K. (eds.), *Advances in Neural Information Processing Systems*, 2022. URL <https://openreview.net/forum?id=wt7cd9m2cz2>.
- [10] Bonnaire, T., Ghio, D., Krishnamurthy, K., Mignacco, F., Yamamura, A., and Biroli, G. High-dimensional non-convex landscapes and gradient descent dynamics, 2023.
- [11] Bruna, J., Pillaud-Vivien, L., and Zweig, A. On single index models beyond gaussian data, 2023.
- [12] Bun, J., Bouchaud, J. P., and Potters, M. Cleaning large correlation matrices: Tools from random matrix theory. *Physics Reports*, 666:1–109, 2017. ISSN 03701573. doi: 10.1016/j.physrep.2016.10.005.
- [13] Cai, J., Huang, M., Li, D., and Wang, Y. Solving phase retrieval with random initial guess is nearly as good as by spectral initialization. *Applied and Computational Harmonic Analysis*, 58:60–84, 2022. URL <http://arxiv.org/abs/2101.03540>.
- [14] Cai, J.-F., Huang, M., Li, D., and Wang, Y. The global landscape of phase retrieval ii: quotient intensity models. *arXiv e-prints*, pp. 1–41, 2021. URL <http://arxiv.org/abs/2112.07997>.
- [15] Cai, J.-F., Huang, M., Li, D., and Wang, Y. Nearly optimal bounds for the global geometric landscape of phase retrieval. *IOP Publishing*, 39:075011, 2023. doi: 10.1088/1361-6420/acdab7. URL <http://arxiv.org/abs/2204.09416><http://dx.doi.org/10.1088/1361-6420/acdab7>.
- [16] Candès, E. J., Li, X., and Soltanolkotabi, M. Phase retrieval via wirtinger flow: Theory and algorithms. *IEEE Transactions on Information Theory*, 61:1985–2007, 2015. ISSN 00189448. doi: 10.1109/TIT.2015.2399924.
- [17] Castellani, T. and Cavagna, A. Spin-glass theory for pedestrians. *Journal of Statistical Mechanics: Theory and Experiment*, pp. 215–266, 2005. ISSN 17425468. doi: 10.1088/1742-5468/2005/05/P05012.
- [18] Chen, Y. and Candès, E. J. Solving random quadratic systems of equations is nearly as easy as solving linear systems. *Communications on Pure and Applied Mathematics*, 70:822–883, 2017. ISSN 10970312. doi: 10.1002/cpa.21638.
- [19] Fienup, J. R. Phase retrieval for image reconstruction. In *Imaging and Applied Optics 2019 (COSI, IS, MATH, pcAOP)*, pp. CM1A.1. Optica Publishing Group, 2019. doi: 10.1364/COSI.2019.CM1A.1. URL <https://opg.optica.org/abstract.cfm?URI=COSI-2019-CM1A.1>.
- [20] Fraboul, J., Biroli, G., and De Monte, S. Artificial selection of communities drives the emergence of structured interactions. *Journal of Theoretical Biology*, 571:111557, 2023.
- [21] Franz, S., Parisi, G., Sevelev, M., Urbani, P., and Zamponi, F. Universality of the sat-unsat (jamming) threshold in non-convex continuous constraint satisfaction problems. *SciPost Physics*, 2:1–37, 2017. ISSN 25424653. doi: 10.21468/SciPostPhys.2.3.019.

- [22] Fyodorov, Y. V. Complexity of random energy landscapes, glass transition, and absolute value of spectral determinant of random matrices. *Physical Review Letters*, 93:149901–149901, 2004. ISSN 00319007. doi: 10.1103/PhysRevLett.93.149901.
- [23] Ghorbani, B., Krishnan, S., and Xiao, Y. An investigation into neural net optimization via hessian eigenvalue density. In Chaudhuri, K. and Salakhutdinov, R. (eds.), *Proceedings of the 36th International Conference on Machine Learning*, volume 97 of *Proceedings of Machine Learning Research*, pp. 2232–2241. PMLR, 09–15 Jun 2019. URL <https://proceedings.mlr.press/v97/ghorbani19b.html>.
- [24] Harrison, R. W. Phase problem in crystallography. *Journal of the Optical Society of America Part A*, 10:1046–1055, 5 1993. doi: 10.1364/JOSAA.10.001046. URL <http://opg.optica.org/josaa/abstract.cfm?URI=josaa-10-5-1046>.
- [25] Li, Z., Cai, J. F., and Wei, K. Toward the optimal construction of a loss function without spurious local minima for solving quadratic equations. *IEEE Transactions on Information Theory*, 66:3242–3260, 2020. ISSN 15579654. doi: 10.1109/TIT.2019.2956922.
- [26] Liu, S., Papailiopoulos, D., and Achlioptas, D. Bad global minima exist and sgd can reach them. In Larochelle, H., Ranzato, M., Hadsell, R., Balcan, M., and Lin, H. (eds.), *Advances in Neural Information Processing Systems*, volume 33, pp. 8543–8552. Curran Associates, Inc., 2020. URL [https://proceedings.neurips.cc/paper\\_files/paper/2020/file/618491e20a9b686b79e158c293ab4f91-Paper.pdf](https://proceedings.neurips.cc/paper_files/paper/2020/file/618491e20a9b686b79e158c293ab4f91-Paper.pdf).
- [27] Lu, Y. M. and Li, G. Phase transitions of spectral initialization for high-dimensional non-convex estimation. *Information and Inference: A Journal of the IMA*, 9:507–541, 2020. ISSN 2049-8772. doi: 10.1093/imaiai/iaz020.
- [28] Luo, Q., Lin, S., and Wang, H. A composite initialization method for phase retrieval. *Symmetry*, 13, 2021. ISSN 20738994. doi: 10.3390/sym13112006. URL <https://www.mdpi.com/2073-8994/13/11/2006/htm>.
- [29] Luo, W., Alghamdi, W., and Lu, Y. M. Optimal spectral initialization for signal recovery with applications to phase retrieval. *IEEE Transactions on Signal Processing*, 67:2347–2356, 2019. doi: 10.1109/TSP.2019.2904918. URL <https://arxiv.org/abs/1811.04420>.
- [30] Ma, S., Bassily, R., and Belkin, M. The power of interpolation: Understanding the effectiveness of sgd in modern over-parametrized learning. In *International Conference on Machine Learning*, pp. 3325–3334. PMLR, 2018.
- [31] Maillard, A., Ben Arous, G., and Biroli, G. Landscape complexity for the empirical risk of generalized linear models. In Lu, J. and Ward, R. (eds.), *Proceedings of The First Mathematical and Scientific Machine Learning Conference*, volume 107 of *Proceedings of Machine Learning Research*, pp. 287–327. PMLR, 20–24 Jul 2020. URL <https://proceedings.mlr.press/v107/maillard20a.html>.
- [32] Maillard, A., Loureiro, B., Krzakala, F., and Zdeborová, L. Phase retrieval in high dimensions: Statistical and computational phase transitions. *Advances in Neural Information Processing Systems*, 33:11071–11082, 2020.
- [33] Maillard, A., Krzakala, F., Lu, Y. M., and Zdeborová, L. Construction of optimal spectral methods in phase retrieval. In *Mathematical and Scientific Machine Learning*, pp. 693–720. PMLR, 2022.
- [34] Mannelli, S. S., Biroli, G., Cammarota, C., Krzakala, F., and Zdeborová, L. Who is afraid of big bad minima? analysis of gradient-flow in a spiked matrix-tensor model. *Advances in Neural Information Processing Systems*, 32:1–28, 2019. ISSN 10495258.
- [35] Mannelli, S. S., Krzakala, F., Urbani, P., and Zdeborová, L. Passed and spurious: Descent algorithms and local minima in spiked matrix-tensor models. In Chaudhuri, K. and Salakhutdinov, R. (eds.), *Proceedings of the 36th International Conference on Machine Learning*, volume 97 of *Proceedings of Machine Learning Research*, pp. 4333–4342. PMLR, 09–15 Jun 2019. URL <https://proceedings.mlr.press/v97/mannelli19a.html>.
- [36] Mannelli, S. S., Biroli, G., Cammarota, C., Krzakala, F., Urbani, P., and Zdeborová, L. Complex dynamics in simple neural networks: Understanding gradient flow in phase retrieval. *Advances in Neural Information Processing Systems*, pp. 1–17, 2020. ISSN 10495258.

- [37] Mannelli, S. S., Biroli, G., Cammarota, C., Krzakala, F., Urbani, P., and Zdeborová, L. Marvels and pitfalls of the langevin algorithm in noisy high-dimensional inference. *Physical Review X*, 10:1–45, 2020. ISSN 21603308. doi: 10.1103/PhysRevX.10.011057.
- [38] Mannelli, S. S., Vanden-Eijnden, E., and Zdeborová, L. Optimization and generalization of shallow neural networks with quadratic activation functions. *Advances in Neural Information Processing Systems*, 2020-Decem:1–26, 2020. ISSN 10495258.
- [39] Martin, S., Bach, F., and Biroli, G. On the impact of overparameterization on the training of a shallow neural network in high dimensions. *arXiv preprint arXiv:2311.03794*, 2023.
- [40] Miao, J., Ishikawa, T., Shen, Q., and Earnest, T. Extending x-ray crystallography to allow the imaging of noncrystalline materials, cells, and single protein complexes. *Annual Review of Physical Chemistry*, 59: 387–410, 2008. ISSN 0066426X. doi: 10.1146/annurev.physchem.59.032607.093642.
- [41] Mignacco, F., Urbani, P., and Zdeborová, L. Stochasticity helps to navigate rough landscapes: Comparing gradient-descent-based algorithms in the phase retrieval problem. *Machine Learning: Science and Technology*, 2, 2021. ISSN 26322153. doi: 10.1088/2632-2153/ac0615.
- [42] Millane, R. P. Phase retrieval in crystallography and optics. *Journal of the Optical Society of America Part A*, 7:394–411, 3 1990. doi: 10.1364/JOSAA.7.000394. URL <http://opg.optica.org/josaa/abstract.cfm?URI=josaa-7-3-394>.
- [43] Mondelli, M. and Montanari, A. Fundamental limits of weak recovery with applications to phase retrieval. *Foundations of Computational Mathematics*, 19:703–773, 2019. ISSN 16153383. doi: 10.1007/s10208-018-9395-y.
- [44] Netrapalli, P., Jain, P., and Sanghavi, S. Phase retrieval using alternating minimization. *IEEE Transactions on Signal Processing*, 63:4814–4826, 2015. ISSN 1053587X. doi: 10.1109/TSP.2015.2448516. URL <https://arxiv.org/abs/1306.0160>.
- [45] Neyshabur, B., Bhojanapalli, S., McAllester, D., and Srebro, N. Exploring generalization in deep learning. In *Proceedings of the 31st International Conference on Neural Information Processing Systems, NIPS’17*, pp. 5949–5958, Red Hook, NY, USA, 2017. Curran Associates Inc. ISBN 9781510860964.
- [46] Pardalos, P. M. and Vavasis, S. A. Quadratic programming with one negative eigenvalue is np-hard. *Journal of Global Optimization*, 1:15–22, 1991. ISSN 09255001. doi: 10.1007/BF00120662. URL <https://doi.org/10.1007/BF00120662>.
- [47] Péché, S. Non-white wishart ensembles. *Journal of Multivariate Analysis*, 97:874–894, 2006. ISSN 0047259X. doi: 10.1016/j.jmva.2005.09.001.
- [48] Ros, V., Arous, G. B., Biroli, G., and Cammarota, C. Complex energy landscapes in spiked-tensor and simple glassy models: Ruggedness, arrangements of local minima, and phase transitions. *Physical Review X*, 9:11003, 2019. ISSN 21603308. doi: 10.1103/PhysRevX.9.011003. URL <https://doi.org/10.1103/PhysRevX.9.011003>.
- [49] Saade, A., Krzakala, F., and Zdeborová, L. Spectral clustering of graphs with the bethe hessian. *Advances in Neural Information Processing Systems*, 27:406–414, 2014. URL <https://proceedings.neurips.cc/paper/2014/file/63923f49e5241343aa7acb6a06a751e7-Paper.pdf>.
- [50] Shechtman, Y., Eldar, Y. C., Cohen, O., Chapman, H. N., Miao, J., and Segev, M. Phase retrieval with application to optical imaging. *arXiv e-prints*, pp. 1–25, 2014. URL <http://arxiv.org/abs/1402.7350>.
- [51] Soudry, D. and Carmon, Y. No bad local minima: Data independent training error guarantees for multilayer neural networks. *arXiv preprint arXiv:1605.08361*, 2016.
- [52] Sun, J., Qu, Q., and Wright, J. A geometric analysis of phase retrieval. *Foundations of Computational Mathematics*, 18:1131–1198, 2018. ISSN 16153383. doi: 10.1007/s10208-017-9365-9.
- [53] Sun, R.-Y. Optimization for deep learning: An overview. *Journal of the Operations Research Society of China*, 8(2):249–294, 2020.

- [54] Venturi, L., Bandeira, A. S., and Bruna, J. Spurious valleys in one-hidden-layer neural network optimization landscapes. *Journal of Machine Learning Research*, 20(133):1–34, 2019. URL <http://jmlr.org/papers/v20/18-674.html>.
- [55] Waldspurger, I., D’Aspremont, A., and Mallat, S. Phase recovery, maxcut and complex semidefinite programming. *Mathematical Programming*, 149:47–81, 2015. ISSN 14364646. doi: 10.1007/s10107-013-0738-9.
- [56] Wang, G., Giannakis, G. B., and Chen, J. Solving large-scale systems of random quadratic equations via stochastic truncated amplitude flow. *25th European Signal Processing Conference, EUSIPCO 2017*, 2017-Janua:1420–1424, 2017. doi: 10.23919/EUSIPCO.2017.8081443.
- [57] Wang, G., Giannakis, G. B., Saad, Y., and Chen, J. Solving most systems of random quadratic equations. *Advances in Neural Information Processing Systems*, 2017-Decem:1868–1878, 2017. ISSN 10495258.
- [58] Wong, A., Pope, B., Desdoigts, L., Tuthill, P., Norris, B., and Betters, C. Phase retrieval and design with automatic differentiation: tutorial. *Journal of the Optical Society of America B*, 38:2465, 2021. ISSN 0740-3224. doi: 10.1364/josab.432723.
- [59] Yao, Z., Gholami, A., Shen, S., Mustafa, M., Keutzer, K., and Mahoney, M. Adahessian: An adaptive second order optimizer for machine learning. *Proceedings of the AAAI Conference on Artificial Intelligence*, 35(12):10665–10673, May 2021. doi: 10.1609/aaai.v35i12.17275. URL <https://ojs.aaai.org/index.php/AAAI/article/view/17275>.
- [60] Zamponi, F. Mean-field theory of spin-glasses. *arXiv e-prints*, 2010. URL <https://arxiv.org/abs/1008.4844>.
- [61] Zhang, C., Wang, M., Chen, Q., Wang, D., and Wei, S. Two-step phase retrieval algorithm using single-intensity measurement. *International Journal of Optics*, 2018, 2018. ISSN 16879392. doi: 10.1155/2018/8643819.
- [62] Zhang, H., Zhou, Y., Liang, Y., and Chi, Y. A nonconvex approach for phase retrieval: Reshaped wirtinger flow and incremental algorithms. *Journal of Machine Learning Research*, 18:1–35, 2017. ISSN 15337928. URL <https://jmlr.org/papers/v18/16-572.html>.



## A Random matrix analysis of the Hessian

### A.1 Characterizing the eigenspectrum and BBP transition

Omitting the spherical constraint – which is just a translation of the eigensupport – the Hessian matrix can be written as a sum of  $M$  free matrices (when ignoring the potential outlier eigenvalue),

$$\mathcal{H}(\mathbf{w}^{(t)}) = \sum_{i=1}^M \mathbf{X}^{(i)}, \quad (10)$$

with  $\mathbf{X}^{(i)} = f(y_i, \hat{y}_i) \mathbf{x}_i \mathbf{x}_i^\top$ . To evaluate the limiting Stieltjes transform of  $\mathcal{H}$ , denoted  $\mathcal{S}_{\mathcal{H}}$ , we use the properties of the R-transform for free random matrices

$$R_{\mathcal{H}} = \sum_{i=1}^M R^{(i)}, \quad (11)$$

with  $R^{(i)} = z - 1/\mathcal{S}^{(i)}$  the R-transform of  $\mathbf{X}^{(i)}$ . For one matrix  $\mathbf{X}^{(i)}$ , the Stieltjes transform yields, by definition,

$$\mathcal{S}^{(i)}(z) = \frac{1}{N} \sum_{i=1}^N \frac{1}{z - \gamma_i}, \quad (12)$$

where  $\gamma_i$  are the eigenvalues of  $\mathbf{X}^{(i)}$ . Since it is a rank-one matrix, its eigenvalues are 0 with multiplicity  $N - 1$  and  $f(y_i, \hat{y}_i)$  with multiplicity one, leading to

$$\mathcal{S}^{(i)}(z) = \frac{1}{z} - \frac{1}{Nz} + \frac{1}{N(z - f(y_i, \hat{y}_i))}. \quad (13)$$

We now need to reverse this relation to obtain  $z$  as a function of  $\mathcal{S}$ . In the large  $N$  limit,  $\mathcal{S}^{(i)}(z) = 1/z$  and we use this to obtain, in the high-dimensional limit,

$$z = \frac{1}{\mathcal{S}^{(i)} \left( 1 + \frac{1}{N} \left[ 1 - \frac{1}{1 - f(y_i, \hat{y}_i) \mathcal{S}^{(i)}} \right] \right)}. \quad (14)$$

At first order in  $1/N$ , we can hence write

$$z = \frac{1}{\mathcal{S}^{(i)}} + \frac{1}{N} \left[ \frac{f(y_i, \hat{y}_i)}{1 - f(y_i, \hat{y}_i) \mathcal{S}^{(i)}} \right] + O\left(\frac{1}{N}\right). \quad (15)$$

The R-transform of  $\mathbf{X}^{(i)}$  is therefore

$$R^{(i)} = \frac{1}{N} \left[ \frac{f(y_i, \hat{y}_i)}{1 - f(y_i, \hat{y}_i) \mathcal{S}^{(i)}} \right]. \quad (16)$$

When  $N \rightarrow \infty$ , the R-transform is expected to concentrate around its mean and we get

$$R_{\mathcal{H}} \xrightarrow{N \rightarrow \infty} \alpha \mathbb{E}_{y, \hat{y}} \left[ \frac{f(y, \hat{y})}{1 - f(y, \hat{y}) \mathcal{S}_{\mathcal{H}}(z)} \right], \quad (17)$$

with  $f(y, \hat{y}) = \partial_{\hat{y}} \ell(y, \hat{y})$ . This finally leads to the following self-consistent equation on the Stieltjes transform of the continuous bulk,

$$\mathcal{S}_{\mathcal{H}}(z)^{-1} = z - \alpha \mathbb{E}_{y, \hat{y}} \left[ \frac{f(y, \hat{y})}{1 - f(y, \hat{y}) \mathcal{S}_{\mathcal{H}}(z)} \right], \quad (18)$$

where the expectation is taken over the joint probability distribution at time  $t$  of  $y$  and  $\hat{y}$  that we denote  $p(y, \hat{y}, t)$ . This equation fully characterizes the bulk of the eigenspectrum through the Sokhotski–Plemelj inversion formula allowing to recover the density of eigenvalues  $\rho(\lambda)$ , as used to obtain Fig. 2.

As argued in the main text, in the presence of an outlier eigenvalue due to the signal the Hessian can be written as the sum of two contributions: one component independent from the signal – the continuous bulk characterized by Eq. (18) – and another component aligned with the signal. Using the rotational invariance

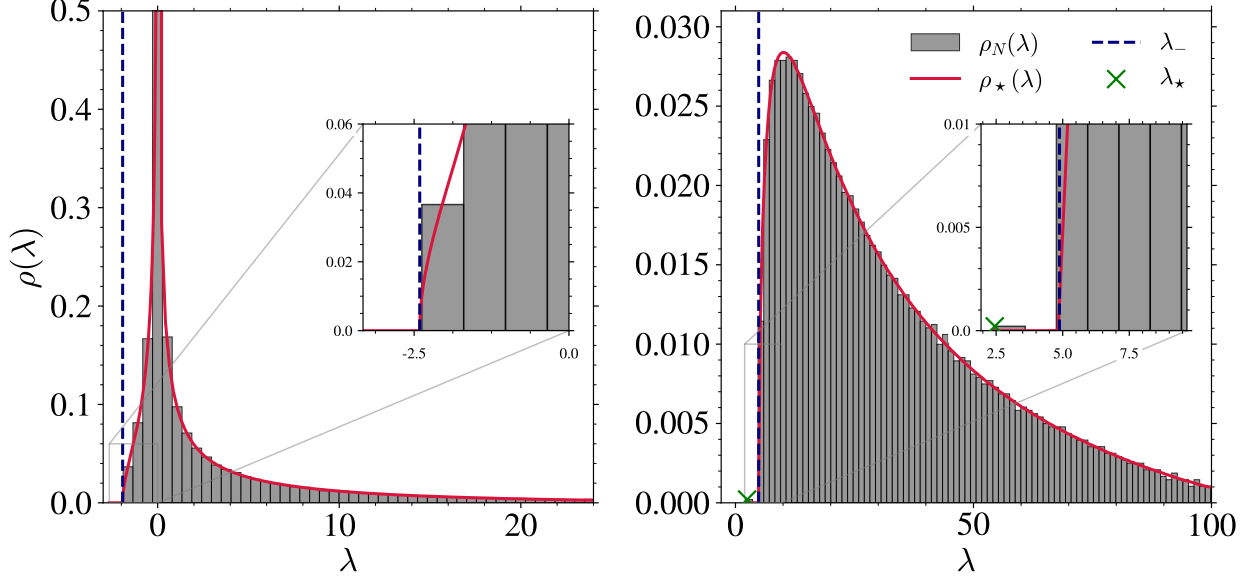


**Figure 6:** Illustrative comparison of the eigenspectrum properties analytically predicted from Eqs. (18), (5), and (6) with empirical spectra. Eigenvalues are obtained at  $t = 0$  (initialization) for  $N = 4096$ ,  $a = 1$ , and (Left)  $\alpha = 1$  or (Right)  $\alpha = 10$ .

of the problem it yields that the outlier eigenvalue  $\lambda_*$  fulfills [27]

$$\lambda_* = \Sigma(\lambda_*), \quad (19)$$

with  $\Sigma(z)$  defined in Eq. (8) as

$$\Sigma(z) = \alpha \mathbb{E}_{y, \hat{y}} \left[ \frac{f(y, \hat{y}) y^2}{1 - f(y, \hat{y}) \mathcal{S}_{\mathcal{H}}(z)} \right]. \quad (20)$$

This holds as long as  $\lambda_* < \lambda_-$ , with  $\lambda_-$  the left edge of the continuous part of the spectrum. A condition on  $\lambda_-$  can be found through the maximum of  $z(\mathcal{S})$ , satisfying

$$\frac{\partial z(\mathcal{S})}{\partial \mathcal{S}} \Big|_{\mathcal{S}=\mathcal{S}_-} = 0. \quad (21)$$

Since  $z(\mathcal{S}) = R_{\mathcal{H}}(\mathcal{S}) + 1/\mathcal{S}$ , we find that

$$\mathcal{S}_- = \left( \mathbb{E}_{y, \hat{y}} \left[ \frac{\alpha^2 f(y, \hat{y})^2}{(1 - f(y, \hat{y}) \mathcal{S}_-)^2} \right] \right)^{-1/2}, \quad (22)$$

which is the condition of the Stieltjes transform of the left edge. Finally, by equating the left edge and the outlier eigenvalue equations, we obtain the BBP condition from Eq. (5), i.e.

$$\lambda_* = \alpha_{\text{BBP}} \mathbb{E}_{y, \hat{y}} \left[ \frac{f(y, \hat{y}) y^2}{1 - f(y, \hat{y}) \mathcal{S}_-} \right], \quad (23)$$

## A.2 Numerical validation of the random matrix equations

Let us now check the accuracy of our approach through a numerical experiment. Figure 6 shows two realizations of matrices in the form of Eq. (4) for  $N = 4096$  with either  $\alpha = 1$  on the left panel or  $\alpha = 10$  on the right panel. The limiting spectra obtained using Eq. (18) are plotted as solid red lines and are perfectly fitting the two empirical distributions, together with their left-most edge characterized by the vertical dashed blue lines and obtained from Eq. (22). The figure also depicts two regimes. In the left panel, the value of  $\alpha$  is too small to observe an outlier outside of the bulk. In the right panel, an eigenvalue pops out of the continuous part of the Hessian spectrum, characteristic of the BBP transition that we analytically quantify in

this appendix. This outlier eigenvalue is correctly predicted by Eq. (19) as shown by the green cross in the figure.

### A.3 Derivation of the overlap

To compute the squared overlap, let us first remark that the problem is invariant by rotation, hence we can focus only on computing the first component of the Stieltjes transform and we can decompose  $\mathcal{S}_{11}(z)$  using the eigenvector  $\mathbf{v}_i$  of  $\mathcal{H}$  as

$$\mathcal{S}_{11}(z) = \sum_{i=1}^N \frac{|[\mathbf{v}_i]_1|^2}{z - \lambda_i}. \quad (24)$$

Noting  $\mathbf{v}_1$  the eigenvector associated to the outlier eigenvalue  $\lambda_*$ , we have

$$\lim_{z \rightarrow \lambda_*} \mathcal{S}_{11}(z) = \frac{(\mathbf{v}_1^\top \mathbf{w}^*)^2}{z - \lambda_*}. \quad (25)$$

By l'Hospital's rule,

$$(\mathbf{v}_1^\top \mathbf{w}^*)^2 = \lim_{z \rightarrow \lambda_*} \frac{z - \lambda_*}{z - \Sigma(z)} = \frac{1}{1 - \partial_z \Sigma(z)|_{z=\lambda_*}}, \quad (26)$$

where  $\Sigma(z)$  is given in Eq. (8).

## B Replica method for the computation of $p(y, \hat{y}, t_{\text{TS}})$

Let us first write the Boltzmann distribution associated to the system as

$$P(\mathbf{w}) = \frac{1}{Z(\beta)} \exp\{-\beta \mathcal{L}(\mathbf{w})\}, \quad (27)$$

where we write  $\mathbf{w}$  as shorthand notation for  $\mathbf{w}^{(t)}$ .  $Z(\beta)$  is the partition function and  $\mathcal{L}(\mathbf{w})$  is the *energy* or *cost function*. The corresponding free energy per particle is

$$\phi(\beta) = -\frac{1}{N\beta} \log Z(\beta), \quad (28)$$

which is tightly coupled with some interesting macroscopic quantities of the system, like the average loss function, the expected overlap, but also to the joint probability distribution  $p(y, \hat{y}, t)$  of true and estimated labels. As first explained in [21] and also exploited in [38], the typical distribution is given by  $p(y, \hat{y}, t) = \mathbb{E}_{\mathbf{w}} [\hat{p}(y, \hat{y}, t)]$ , where  $\hat{p}$  denotes the empirical measure, the overline is the average over the disorder (here the dataset  $\{\mathbf{x}_m\}_{m=1}^M$ ), and the expectation is taken over the Boltzmann measure. The partition function can be written in terms of  $\hat{p}(y, \hat{y}, t)$  as

$$\overline{Z(\beta)} = \overline{\int_{\mathbb{S}^{N-1}} d\mathbf{w} \exp\{-\beta \mathcal{L}(\mathbf{w})\}}, \quad (29)$$

$$= \overline{\int_{\mathbb{S}^{N-1}} d\mathbf{w} \exp\left\{-\frac{\beta}{2} \sum_{m=1}^M \ell(y_m, \hat{y}_m)\right\}}, \quad (30)$$

$$= \overline{\int_{\mathbb{S}^{N-1}} d\mathbf{w} \exp\left\{-\frac{\beta M}{2} \int dy d\hat{y} \ell(y, \hat{y}) \hat{p}(y, \hat{y}, t)\right\}}. \quad (31)$$

From this last expression, the distribution  $p(y, \hat{y}, t)$  is accessible through the functional derivative of the free energy as

$$\frac{\delta \overline{\phi}}{\delta \ell(y, \hat{y})} = -\frac{1}{N\beta} \frac{\delta \overline{\log Z(\beta)}}{\delta \ell(y, \hat{y})} = \frac{\alpha}{2} \mathbb{E}_{\mathbf{w}} [\hat{p}(y, \hat{y}, t)] = \frac{\alpha}{2} p(y, \hat{y}, t). \quad (32)$$

This gives us some motivation for the computation of the log partition function, and more precisely its first moment if we can expect large deviation principle to apply to obtain the "typical" behavior of the system.

## B.1 Replicated partition function

To compute the average free energy per particle, we can use the replica method stating that

$$\overline{\log Z} = \lim_{n \rightarrow 0} \frac{\overline{Z^n} - 1}{n}. \quad (33)$$

In practice, we will compute  $\overline{Z^n}$  for  $n \in \mathbb{N}$  and then analytically continue it to  $n \in \mathbb{R}$  in order to finally take the  $n \rightarrow 0$  limit. The problem now boils down to compute  $\overline{Z^n}$  which can be expressed as the partition function associated to the product of  $n$  independent systems with the partition function  $Z(\beta)$  and gives

$$Z(\beta)^n = \int_{\mathbb{S}^{N-1}} \prod_{a=1}^n \left[ d\mathbf{w} \exp \left\{ -\beta \sum_{m=1}^M \ell(\mathbf{x}_m \cdot \mathbf{w}^*, \mathbf{x}_m \cdot \mathbf{w}) \right\} \right]. \quad (34)$$

Let us introduce  $r_m^{(a)} = \mathbf{x}_i \cdot \mathbf{w}^{(a)}$ , the overlap between the entries and the state of the  $a^{\text{th}}$  system, reserving the index zero for the overlap with the ground truth, meaning with  $r_m^{(0)} = \mathbf{x}_i^T \mathbf{w}^*$ . These new variables are introduced through delta functions that we replace by their Fourier representation. We therefore get

$$Z(\beta)^n \propto \int_{\mathbb{S}^{N-1}} \prod_{a=1}^n d\mathbf{w}^{(a)} \int \prod_{a=0}^n \prod_{m=1}^M dr_m^{(a)} \int \prod_{a=0}^n \prod_{m=1}^M d\hat{r}_m^{(a)} \exp \left\{ -\beta \sum_{a=1}^n \sum_{m=1}^M \ell(r_m^{(0)}, r_m^{(a)}) + i \sum_{a=0}^n \sum_{m=1}^M \hat{r}_m^{(a)} r_m^{(a)} + i \sum_{a=0}^n \sum_{m=1}^M \hat{r}_m^{(a)} \mathbf{x}_i \cdot \mathbf{w}^{(a)} \right\}. \quad (35)$$

This allows us to compute the expectation over the disorder since, now, it only acts on the last term in the exponential. This integral can be evaluated using the Hubbard-Stratonovich identity<sup>2</sup> as

$$E(X) = \mathbb{E}_{\mathbf{X}} \left[ \exp \left\{ i \sum_{a=0}^n \sum_{m=1}^M \hat{r}_m^{(a)} \mathbf{x}_i \cdot \mathbf{w}^{(a)} \right\} \right], \quad (36)$$

$$\propto \exp \left\{ -\frac{1}{2N} \sum_{a,b=0}^n \sum_{m=1}^M \hat{r}_m^{(a)} \hat{r}_m^{(b)} \mathbf{w}^{(a)} \cdot \mathbf{w}^{(b)} \right\}. \quad (37)$$

Let us now consider the overlap between two replicas,  $q_{ab} = \frac{1}{N} \mathbf{w}^{(a)} \cdot \mathbf{w}^{(b)}$ . In the same way as previously, we use the index zero for the overlap with the signal  $\mathbf{w}^*$  such that  $\forall a \in [1, n], q_{0a} = m$  and we also have  $\forall a \in [0, n], q_{aa} = 1$ . All these overlaps are regrouped into an  $(n+1) \times (n+1)$  matrix  $\mathbf{Q}$  and are introduced through a delta function again. It then reads

$$\begin{aligned} \overline{Z(\beta)^n} \propto & \int \prod_{0 \leq a \leq b \leq n} dq_{ab} \int \prod_{a=0}^n \prod_{m=1}^M dr_m^{(a)} \int \prod_{a=0}^n \prod_{m=1}^M d\hat{r}_m^{(a)} \\ & \underbrace{\int_{\mathbb{S}^{N-1}} \prod_{a=1}^n d\mathbf{w}^{(a)} \prod_{0 \leq a \leq b \leq n} \delta(Nq_{ab} - \mathbf{w}^{(a)} \cdot \mathbf{w}^{(b)})}_{J(\mathbf{Q})} \\ & \exp \left\{ -\beta \sum_{a=1}^n \sum_{m=1}^M \ell(r_m^{(0)}, r_m^{(a)}) + i \sum_{a=0}^n \sum_{m=1}^M \hat{r}_m^{(a)} r_m^{(a)} - \frac{1}{2} \sum_{a,b=0}^n \sum_{m=1}^M \hat{r}_m^{(a)} \hat{r}_m^{(b)} q_{ab} \right\}, \quad (38) \end{aligned}$$

<sup>2</sup>Stating that  $\int \exp\{-ax^2 + bx\} dx = \sqrt{\pi/a} \exp\{b^2/4a\}$ .

with  $J(\mathbf{Q}) = |\mathbf{Q}|^{N/2}$  in the large  $N$  limit [60], consequently giving, after factorizing the  $M$  integrals

$$\overline{Z(\beta)^n} \propto \int \prod_{0 \leq a \leq b \leq n} dq_{ab} \exp \left\{ \frac{N}{2} \log |\mathbf{Q}| \right\} \left[ \int \prod_{a=0}^n dr^{(a)} \int \prod_{a=0}^n d\hat{r}^{(a)} \exp \left\{ -\beta \sum_{a=1}^n \ell \left( r^{(0)}, r^{(a)} \right) + i \sum_{a=0}^n \hat{r}^{(a)} r^{(a)} - \frac{1}{2} \sum_{a,b=0}^n \hat{r}^{(a)} \hat{r}^{(b)} q_{ab} \right\} \right]^M. \quad (39)$$

Performing the integral over  $\hat{r}$  using the Hubbard-Stratonovich identity again and setting  $N \rightarrow \infty$ , we finally obtain the replicated partition function

$$\overline{Z(\beta)^n} \propto \exp \left\{ N \text{extr}_{\mathbf{Q}} S(\mathbf{Q}) \right\}, \quad (40)$$

with

$$S(\mathbf{Q}) = \frac{1}{2} \log |\mathbf{Q}| + \alpha \log \int \prod_{a=0}^n \frac{dr^{(a)}}{(2\pi)^{n/2} \sqrt{|\mathbf{Q}|}} \exp \left\{ -\beta \sum_{a=1}^n \ell \left( r^{(0)}, r^{(a)} \right) - \frac{1}{2} \sum_{a,b} r^{(a)} \mathbf{Q}_{ab}^{-1} r^{(b)} \right\}, \quad (41)$$

$$= S_1 + S_2 \quad (42)$$

where  $S_1$  is an entropic factor counting the number of spherical couplings that satisfies the constraints  $q_{ab} = \mathbf{w}^{(a)} \cdot \mathbf{w}^{(b)} / N$  and  $S_2$  is the energetic contribution specific to the learning rule in which appears the energy function per variable  $\ell$ .

## B.2 One-step replica symmetry breaking (1RSB)

Notice that we turned the initial problem of computing a high-dimensional integral into a high-dimensional optimization over  $(n+1)^2$  variables in Eq. (41). Although this may seem doomed, we can pursue our analytical treatment by using an ansatz on the form of  $\mathbf{Q}$ . The simplest form of hypothesis is replica symmetry assuming  $q_{ab} = q_0$  for  $a \neq b$ . However, this assumption breaks in the regime we are in and one needs to *break the symmetry*. In our case, we use the first level of symmetry breaking (1RSB) assuming

$$\mathbf{Q} = \mathbf{Q}_{1\text{RSB}} = \begin{pmatrix} 1 & m & \cdots & m \\ m & \tilde{\mathbf{Q}} & q_0 & q_0 & q_0 & q_0 \\ & & q_0 & q_0 & q_0 & q_0 \\ \vdots & q_0 & q_0 & \tilde{\mathbf{Q}} & q_0 & q_0 \\ & q_0 & q_0 & & q_0 & q_0 \\ m & q_0 & q_0 & q_0 & q_0 & \tilde{\mathbf{Q}} \\ & q_0 & q_0 & q_0 & q_0 & \end{pmatrix} \in \mathbb{R}^{(n+1) \times (n+1)}, \quad (43)$$

with  $\tilde{\mathbf{Q}}$  a matrix of size  $p \times p$  with one on the diagonal and  $q_1$  everywhere else. Under this assumption, the action can be written in terms of the four parameters  $n, m, p, q_0$  and  $q_1$ . This hence reduces the saddle point method to extremize over those parameters only in Eq. 40. This type of matrix was heavily studied in the statistical physics literature and one result of particular interest for us is to remark that  $\mathbf{Q}_{1\text{RSB}}$  has three eigenvalues  $\tilde{\lambda}_i$  with multiplicities  $d_i$  given by [17]

$$\begin{cases} \tilde{\lambda}_1 = 1 - q_1, & d_1 = n \left( 1 - \frac{1}{p} \right), \\ \tilde{\lambda}_2 = p(q_1 - q_0) + (1 - q_1), & d_2 = \frac{n}{p} - 1, \\ \tilde{\lambda}_3 = p(q_1 - q_0) + (1 - q_1) + n(q_0 - m^2), & d_3 = 1. \end{cases} \quad (44)$$

Using these eigenvalues, we can evaluate the entropy in the action as

$$S_1^{1\text{RSB}}(q_0, q_1, m, p) = \frac{n}{2} \left[ \log(1 - q_1) + \frac{1}{p} \log \frac{1 - q_1 + p(q_1 - q_0)}{1 - q_1} + \frac{q_0 - m^2}{1 - q_1 + p(q_1 - q_0)} \right] + O(n^2). \quad (45)$$



For the energetic term, one has to use the form of  $\mathbf{Q}_{1\text{RSB}}$  to work out that

$$-\frac{1}{2} \sum_{a,b} \hat{r}^{(a)} \hat{r}^{(b)} q_{ab} = -\frac{1}{2} \left[ \hat{r}^{(0)} \hat{r}^{(0)} + (1 - q_1) \sum_{a=1}^n \hat{r}^{(a)} \hat{r}^{(a)} + (q_1 - q_0) \sum_{P_a=1}^{n/p} \left( \sum_{a \in P_a} \hat{r}^{(a)} \right)^2 + q_0 \left( \sum_{a=1}^n \hat{r}^{(a)} \right)^2 + 2m \sum_{a=1}^n r^{(a)} r^{(0)} \right]. \quad (46)$$

Substituting it into  $S_2$  gives

$$S_2^{1\text{RSB}}(q_0, q_1, m, p) \underset{n \rightarrow 0^+}{\approx} \frac{\alpha n}{p} \int d\eta \int dr^{(0)} D(r^{(0)}, \eta) \log \left( \int \frac{d\eta_P}{\sqrt{2\pi(q_1 - q_0)}} \exp \left\{ -\frac{\eta_P^2}{2(q_1 - q_0)} \right\} \left[ \int \frac{dr}{\sqrt{2\pi}} \exp \left\{ -\beta \Psi(r^{(0)}, r, \eta_P, \eta, q_1) \right\} \right]^p \right), \quad (47)$$

where

$$\Psi(r^{(0)}, r, \eta_P, \eta, q_1) = \ell(r^{(0)}, r) + \frac{(\eta_P + \eta - r)^2}{2\beta(1 - q_1)}. \quad (48)$$

### B.3 Zero-temperature limit and free energy

The 1RSB free energy is defined as the zero temperature limit ( $\beta \rightarrow \infty$ ) of the extremum of the 1RSB action  $S^{1\text{RSB}} = S(\mathbf{Q}_{1\text{RSB}})$

$$\phi_{1\text{RSB}} = \lim_{\beta \rightarrow +\infty} \lim_{n \rightarrow 0^+} -\frac{1}{n\beta} S_1^{1\text{RSB}}(q_0, q_1, m, p) - \frac{1}{n\beta} S_2^{1\text{RSB}}(q_0, q_1, m, p). \quad (49)$$

While taking the  $\beta \rightarrow +\infty$  limit, we set  $q_1 \rightarrow 1$  keeping both  $\chi = \beta(1 - q_1)$  and  $z = \beta p$  of order one. Putting it all together, and setting  $m$  to zero by remarking it satisfies the saddle-point  $\partial_m S^{1\text{RSB}} = 0$ , we end up with the 1RSB free energy

$$\phi_{1\text{RSB}}(\chi, z, q_0) = -\frac{1}{2z} \log \frac{\chi + z(1 - q_0)}{\chi} - \frac{1}{2} \frac{q_0}{\chi + z(1 - q_0)} - \frac{\alpha}{z} \int d\eta \int dr^{(0)} D(r^{(0)}, \eta) \log \left( \int \frac{d\eta_P}{\sqrt{2\pi(1 - q_0)}} \exp \left\{ -\frac{\eta_P^2}{2(1 - q_0)} - z \Psi_0(r^{(0)}, \eta_P, \eta, \chi) \right\} \right), \quad (50)$$

with

$$\Psi_0(r^{(0)}, \eta_P, \eta, \chi) = \min_{\tilde{r}} \ell(r^{(0)}, \tilde{r}) + \frac{(\eta_P + \eta - \tilde{r})^2}{2\chi}, \quad (51)$$

$$D(r^{(0)}, \eta) = \frac{1}{2\pi\sqrt{q_0}} \exp \left\{ -\frac{r^{(0)2} q_0 \eta + \eta^2}{2q_0} \right\}. \quad (52)$$

From Eq. (32), we need to take the functional derivative of the free energy with respect to the loss function  $\ell(y, \hat{y})$  to obtain the joint distribution of true and estimated labels on threshold states  $p(y, \hat{y}, t_{\text{TS}})$ . This gives

$$p(y, \hat{y}, t_{\text{TS}}) = \frac{1}{\sqrt{2\pi}} \int \frac{d\eta}{\sqrt{2\pi q_0}} \exp \left\{ -\frac{y^2 q_0 + \eta^2}{2q_0} \right\} \frac{\exp \left\{ -\frac{\hat{y}^2}{2(1 - q_0)} - z \Psi_0(y, \hat{y}, \eta, \chi) \right\}}{\int d\tilde{y} \exp \left\{ -\frac{\tilde{y}^2}{2(1 - q_0)} - z \Psi_0(y, \tilde{y}, \eta, \chi) \right\}}, \quad (53)$$

which is equivalent to the finding of [36] if we set  $q_0 = 0$ . Finally, the parameters  $\chi$ ,  $z$ , and  $q_0$  are fixed via

the saddle-point equations obtained from  $\partial_\chi S^{1\text{RSB}} = 0$  and  $\partial_{q_0} S^{1\text{RSB}} = 0$ , giving

$$\frac{1}{z} \left( \frac{1}{\chi} - \frac{1}{\chi + z(1 - q_0)} \right) + \frac{q_0}{(\chi + z(1 - q_0))^2} = \alpha \int d\eta \int dr^{(0)} D(r^{(0)}, \eta) \frac{\int d\eta_P \exp \left\{ -\frac{\eta_P^2}{2(1 - q_0)} - z\Psi_0(r^{(0)}, \eta_P, \eta, \chi) \right\} (\partial_{\eta_P} \Psi_0(r^{(0)}, \eta_P, \eta, \chi))^2}{\int d\eta_P \exp \left\{ -\frac{\eta_P^2}{2(1 - q_0)} - z\Psi_0(r^{(0)}, \eta_P, \eta, \chi) \right\}}, \quad (54)$$

$$-\frac{q_0}{(\chi + z(1 - q_0))^2} = \frac{2\alpha}{z^2} \int d\eta \int dr^{(0)} D(r^{(0)}, \eta) \frac{\eta^2 - q_0}{2q_0^2} \log \left( \int \frac{d\eta_P}{\sqrt{2\pi(1 - q_0)}} \exp \left\{ -\frac{\eta_P^2}{2(1 - q_0)} - z\Psi_0(r^{(0)}, \eta_P, \eta, \chi) \right\} \right) + \frac{\alpha}{z^2(1 - q_0)} - \frac{\alpha}{z^2(1 - q_0)^2} \int d\eta \int dr^{(0)} D(r^{(0)}, \eta) \frac{\int d\eta_P \exp \left\{ -\frac{\eta_P^2}{2(1 - q_0)} - z\Psi_0(r^{(0)}, \eta_P, \eta, \chi) \right\} \eta_P^2}{\int d\eta_P \exp \left\{ -\frac{\eta_P^2}{2(1 - q_0)} - z\Psi_0(r^{(0)}, \eta_P, \eta, \chi) \right\}}. \quad (55)$$

On the other hand,  $z$  is fixed by the marginality condition of the Hessian spectrum that we assume on threshold states [21, 36], allowing us to obtain the probability distribution for  $t = t_{\text{TS}}$ . Using Eq. (53) in Eqs. (5) and (6) yields the value  $\alpha_{\text{BBP}}^{\text{TS}, 1\text{RSB}} = 6.9$ . We expect that breaking further the symmetry by assuming substructures in  $Q_{1\text{RSB}}$  would reduce the gap with the  $\alpha_{\text{BBP}}^{\text{TS}} = 6.55$  obtained from the sampling of threshold states but leave this aspect for further investigations.

## C Details of the numerical experiments

All the numerical experiments were run on CPUs for  $N \leq 1024$  while on NVIDIA A6000 for  $N \geq 2048$ . Depending on the value of  $N$ ,  $\alpha$ , and on the initialization scheme, it takes between fifteen minutes to sixteen hours to obtain a batch of 100 simulations.

**Effects of hyperparameters on the numerical results.** All the figures of the main text are obtained by fixing  $\eta = 6 \times 10^{-3}$  and performing  $t_c = 60\,000$  steps for the constrained initialization. Our analysis focuses on gradient flow with  $\eta \rightarrow 0$ . In practice, we set  $\eta$  sufficiently small not to have any impact on the presented phenomena. The left panel of Fig. 7 illustrates for instance the strong recovery rates obtained when  $\eta$  is decreased to  $6 \times 10^{-4}$  but keeping the total simulation time  $\eta T$  constant (with  $10t_c$  steps for the constrained initialization). In this case, the dynamical transition is not displaced significantly and is found at around  $\alpha \approx 5.65$ , agreeing with the one in the main text under the error bars. In a similar way, we report in the right panel of Fig. 7 the strong recovery rates obtained by fixing  $\eta$  to its fiducial value of  $6 \times 10^{-3}$ ,  $N = 512$ , and varying  $t_c$  from 15 000 to 120 000. The simulations share the same weights at initialization. When  $t_c$  is above 30 000, we do not see any impact on the strong recovery rates, and hence on the dynamical transition. This shows the robustness of the numerical experiments with respect to those hyperparameters.

**Logarithmic scaling of the strong recovery rates.** In Fig. 8 can be found some evidences of the displacement of the strong recovery rates obtained in Fig. 4 for randomly initialized weights with  $N \in [256, 8192]$ . In this case, the effective transition is shown to increase with  $\log N$ , as a consequence of the local initial curvature coupled with the initial magnetization  $m(0)$  of order  $1/\sqrt{N}$ , as discussed in the main text.

**Numerical estimate of the BBP transition on threshold states.** In Sect. 3 and Sect. 4, we use a numerical approach to extract  $p(y, \hat{y}, t_{\text{TS}})$  and compute  $\alpha_{\text{BBP}}^{\text{TS}}$ . The method relies on sampling the threshold states using the constrained initialization (see Sect. 4.1) to then compute the expectations from Eqs. (5), (6), and (7) by averaging numerically. Of course, this means that we are using finite  $N$  simulations to compute expectations derived for  $N \rightarrow \infty$ . In practice, we use  $N = \{512, 1024, 2048\}$  simulations to perform a finite-size scaling analysis of  $\alpha_{\text{BBP}}^{(t)}$ . We checked that this procedure allows us to retrieve the analytical value of  $\alpha_{\text{BBP}}^{\text{init}} = 1.13$  with great accuracy and obtain on threshold states the value given in the main text of  $\alpha_{\text{BBP}}^{\text{TS}} = 6.55$ . In order to check the consistency with larger values of  $N$ , we also compared this result with hundreds of numerical simulations with  $N = 8192$  leading to the same value.

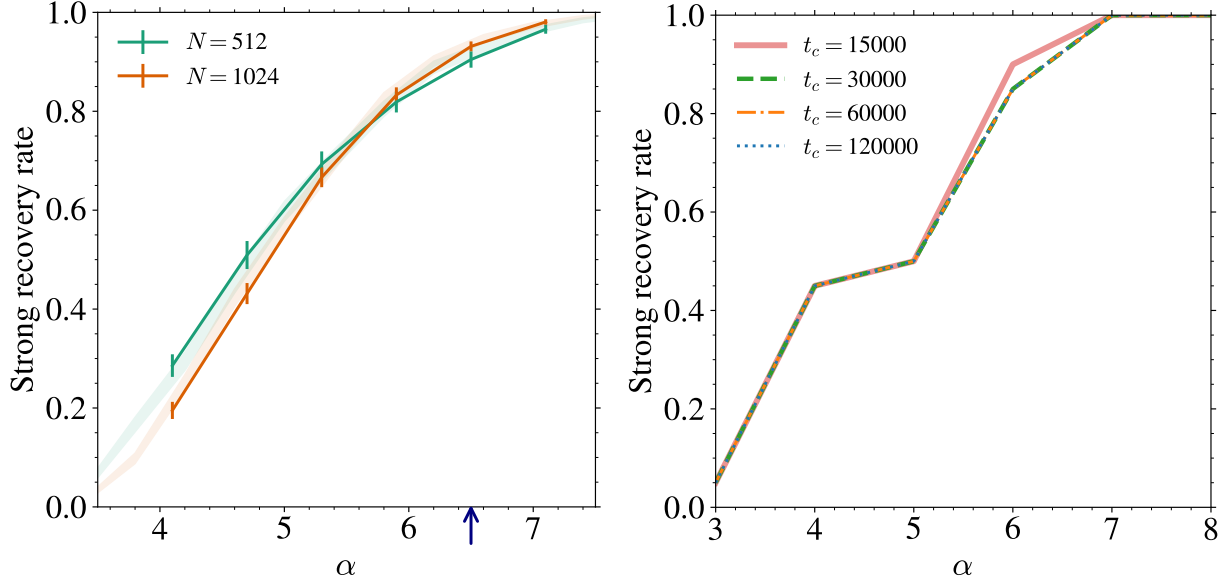


**Figure 7:** (Left) Effect of decreasing the learning rate by a factor ten ( $\eta = 6 \times 10^{-4}$ , solid lines) on the strong recovery rate of the constrained simulations. The shaded areas are the rates obtained with  $\eta = 6 \times 10^{-3}$ , the value used in the main text. The blue arrow indicates  $\alpha_{\text{BBP}}^{\text{TS}}$  computed for  $a = 1$ . (Right) Effect of varying  $t_c$ , the number of steps to approach the threshold states in constrained initialization. When  $t_c > 30\,000$ , they all lead to the same strong recovery rates.

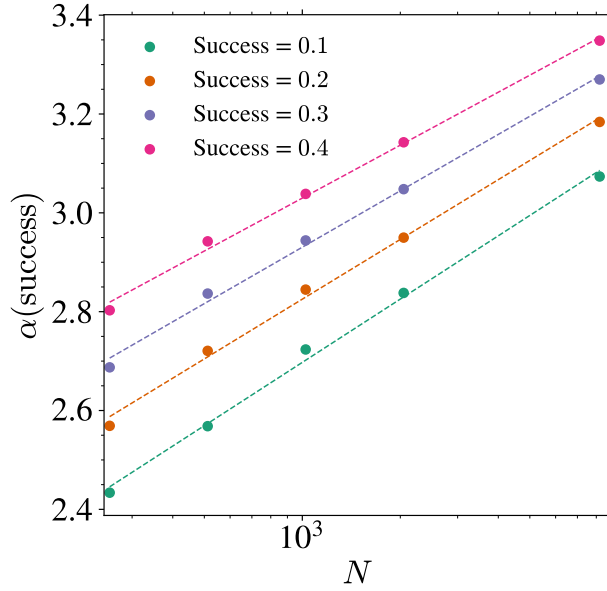


**Figure 8:** Scaling of  $\alpha$  for several fixed strong recovery rates (shown in Fig. 4) for random initializations and  $N \in \{256, 512, 1024, 2048, 8192\}$ .

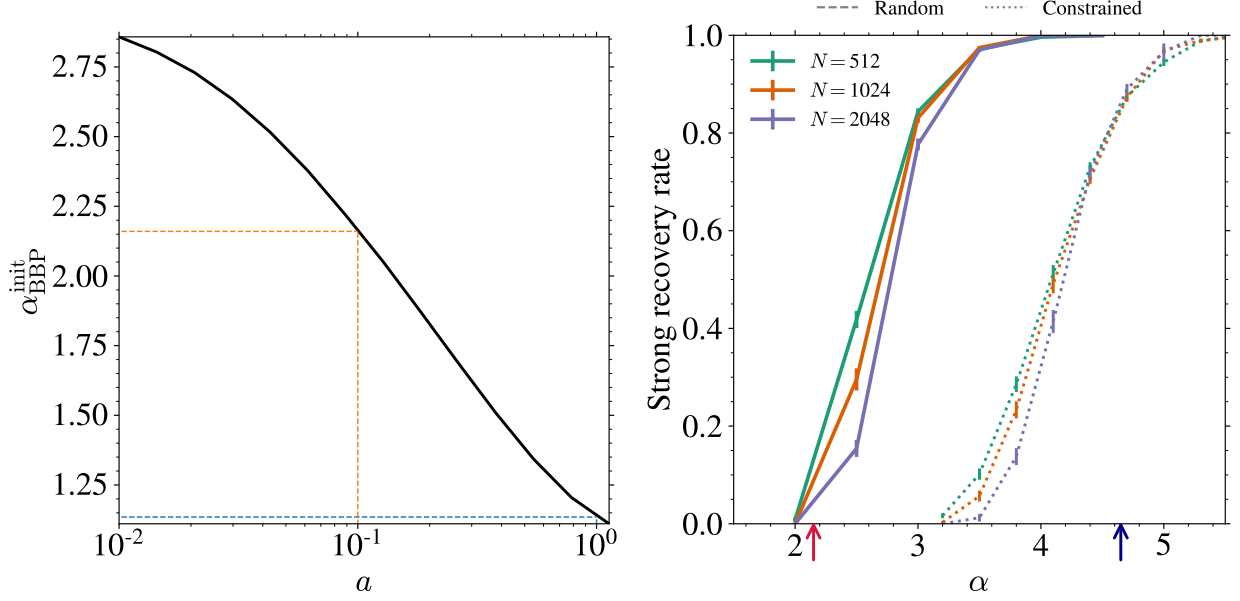


**Figure 9:** (Left) Evolution of  $\alpha_{\text{BBP}}^{\text{init}}$  with  $a$ , the normalization of the loss function (3). The lower  $\alpha_{\text{BBP}}^{\text{init}}$ , the more favorable the landscape at initialization. The two colored dashed lines refer to the values of  $a = 1$  and  $a = 0.1$  discussed throughout the main text and in Appendix D respectively. (Right) Strong recovery rates for the case of a loss function  $\ell_{a=0.1}$  with random and constrained initializations. The red (resp. blue) arrow indicates  $\alpha_{\text{BBP}}^{\text{init}} = 2.15$  (resp.  $\alpha_{\text{BBP}}^{\text{TS}} = 4.65$ ) computed in this case.

## D Impact of the loss function on the BBP transitions

In the main text, we focused on the loss function  $\ell_a(y, \hat{y})$  from Eq. (3) with  $a = 1$ . The precise values of the BBP transitions however depend on the choice of  $\ell$  and some other choice may lead to more favorable landscapes enabling earlier strong recovery. To illustrate this, we plot in the left panel of Fig. 9 the evolution of  $\alpha_{\text{BBP}}^{\text{init}}$  computed for several values of  $a$ . Lowering  $a$  leads to larger  $\alpha_{\text{BBP}}^{\text{init}}$  meaning more samples are required to start having the local curvature towards the signal at initialization. Considering  $a = 0.1$ , we find for instance  $\alpha_{\text{BBP}}^{\text{init}} = 2.16$  and  $\alpha_{\text{BBP}}^{\text{TS}} = 4.65$ . Even though the initial states have a downward direction towards the signal at larger values of the signal-to-noise ratio than for  $a = 1$ , threshold states on their side develop an instability earlier. This is clearly seen in right panel of Fig. 9 where the algorithmic transition occurs earlier than in Fig. 4 for both random and constrained initializations. In this case, we also observe a logarithmic scaling of success rates with  $N$  for random initializations while the curves intersect nicely with the constrained initialization, at around  $\alpha_{\text{cons.}}^{\text{SR}} \approx 4.5$ . This value is also much closer to the  $N \rightarrow \infty$  prediction for this value of  $a$  than for  $a = 1$  used in the main text.